Advanced Composites and Hybrid Materials (2026) 9:277
https://doi.org/10.1007/s42114-026-01820-9

RESEARCH

Toward Filtration-free Contact-electro-catalysis: A robust and recyclable electrospun SiO_2–PVDF Nanofibrous mat for decolorization of organic dyes

Muhammad Awais[1] · Sunmin Jang[2,3] · Donghan Lee[2] · Sumin Cho[2,4] · Sangeun Lee[1] · Soban Ali Shah[2] · Muhammad Ramzan Khawar[2] · Kangmin Yun[2] · Dongik Kam[2] · Juyeong Kim[1] · Hee Jae Hwang[5] · Sung Jea Park[6,7,8] · Dongwhi Choi[1,2]

Received: 16 January 2026 / Revised: 6 April 2026 / Accepted: 17 April 2026

Abstract

Contact-electro-catalysis (CEC) utilizing liquid-solid contact electrification (LS-CE) has demonstrated significant potential for degrading organic pollutants without external electrical bias. While particle-based dielectric materials have shown high catalytic activity, their practical application often necessitates additional post-treatment filtration to recover the catalysts and ensure treated water quality. To streamline this process and enhance operational usability, we developed a filtration-free electrospun SiO_2-PVDF nanofibrous mat (NF-mat). By immobilizing the active SiO_2 and PVDF components within a robust fibrous matrix, this approach effectively circumvents the need for complex recovery steps. Under ultrasonic excitation, the NF-mat provides a hierarchically porous architecture with a high specific surface area (41.6m^2/g), creating an optimal environment for liquid-solid electron transfer and Reactive Oxygen Species (ROS) generation. Consequently, the NF-mat achieved efficient decolorization of both cationic methylene blue (MB, 99.5% within 4h) and anionic methyl orange (MO, 98.1% within 8h). Although MB removal involved a concurrent adsorption contribution, adsorption alone could not account for the near-complete decolorization, and the removal of both MB and MO was predominantly governed by CEC. Furthermore, the mat exhibited excellent mechanical stability and recyclability over multiple cycles without structural disintegration. This study proposes a user-friendly and sustainable platform for CEC-based water treatment, offering a viable solution for continuous environmental remediation.

Muhammad Awais and Sunmin Jang contributed equally to this work.

✉ Sung Jea Park
psj7517@koreatech.ac.kr

✉ Dongwhi Choi
dongwhi.choi@khu.ac.kr

[1] Department of Mechanical Engineering, Kyung Hee University, 1732 Deogyeong-daero, Yongin 17104, Gyeonggi, Republic of Korea

[2] Department of Mechanical Engineering (Integrated Engineering Program), Kyung Hee University, 1732 Deogyeong-daero, Yongin 17104, Gyeonggi, Republic of Korea

[3] Department of Chemical and Biomolecular Engineering, North Carolina State University, Raleigh, NC 27695, USA

[4] Department of Bioengineering, University of California, Los Angeles, Los Angeles, CA, USA

[5] School of Mechanical System Engineering, Kumoh National Institute of Technology, 61, Daehak-ro, Gumi-si 39177, Gyeongsangbuk-do, Republic of Korea

[6] School of Mechanical Engineering, Korea University of Technology and Education, 1600 Chungjeol-ro, Cheonan 31253, Chungnam, Republic of Korea

[7] Advanced Technology Research Centre, Korea University of Technology and Education, 1600 Chungjeol-ro, Cheonan 31253, Chungnam, Republic of Korea

[8] Future Convergence Engineering, Korea University of Technology and Education, 1600 Chungjeol-ro, Cheonan 31253, Chungnam, Republic of Korea

Published online: 29 April 2026

1 Introduction

With the Industrial Revolution, a severe increase in environmental pollution posed a global threat to the ecosystem. An estimated 15% of synthetic dyes are disposed of into the global environment each year, which is responsible for disturbing the ecosystem and contaminating the aquatic life [1]. The polluted water can cause detrimental health effects such as respiratory ailments, gastrointestinal illnesses, and cancer [2]. Particularly, the organic pollutants require more efforts to remove from the contaminated sites due to their complex molecular structure that contains aromatic rings and azo bonds, which make them persistent and low biodegradable species, and also show resistance against conventional treatments [3]. For this purpose, some techniques have been reported to decolorize the organic dyes, such as photocatalytic reduction [4], biodegradation [5], and mechanochemistry catalytic degradation [6, 7]. Consequently, to mitigate the environmental impact of such pollutants, an efficient and reliable remediation strategy becomes imperative.

In this context, Wang et al. [8] first proposed a substantial and new advancement in the field of catalysis known as contact-electro-catalysis (CEC), wherein the generation of free radicals is capable of catalyzing the disintegration of organic contaminants, such as synthetic dyes, without the application of external voltage or current. In this phenomenon, the catalytic reactions commence at the liquid-solid interface, where a frequent contact-separation phenomenon induces interfacial electron transfer between these two species. Consequently, this electron transfer across the liquid-solid (L-S) interface generates the reactive oxygen species (ROS) after subsequent reactions, which facilitates the disintegration of the organic species [9]. In this technique, dielectric polymers such as fluorinated ethylene propylene (FEP), polyvinylidene fluoride (PVDF), Teflon, nylon, and rubber, etc., are deployed as triboelectric materials that undergo liquid-solid contact electrification (LS-CE), enabling interfacial electron withdrawal from water molecules, which promotes the generation of ROS [9, 10]. Moreover, the CEC technique exhibited its effectiveness with a wide spectrum of triboelectric materials, including successful applications with inorganic compounds such as silica (SiO_2) and manganese dioxide (MnO_2), etc., which have also been reported to facilitate the ROS generation [9]. To trigger the frequent but effective LS-CE, the ultrasound of specified power and frequency is vital, which plays a crucial role in producing a desired amount of ROS generation [11, 12].

Enhancing contact electrification (CE) is crucial for maximizing the efficiency of CEC. Consequently, fluoropolymers such as PVDF, FEP, and polytetrafluoroethylene (PTFE) have garnered significant attention for CEC applications due to their superior hydrophobicity and high electron affinity—key properties for effective liquid-solid CE (LS-CE). While various fluoropolymer films and particles have been employed to decolorize organic compounds, the catalytic reaction rate is intrinsically limited by the liquid-solid contact area. To address this and maximize the density of the effective LS-CE interface, recent research has increasingly focused on utilizing fluoropolymer particles. Nonetheless, the particle-based CEC requires pre-treatment and constant spinning for 24–48 h, and particularly, the post-treatment filtering process is also essential [9–11]. Post-reaction filtration is essentially a labor-intensive and time-consuming bottleneck. More importantly, given that fluoropolymers—specifically polyfluoroalkyl substances (PFAS)—are increasingly regulated due to their environmental persistence and bioaccumulation, any inadequacy in filtration poses a severe risk. Incomplete removal may lead to the release of residual nanoparticles into the ecosystem, causing secondary pollution that undermines the remediation efforts [13]. To overcome the aforementioned issue, it is essential to develop effective CEC material with remarkable CEC efficiency that can mitigate secondary pollution without the need for additional post-processing steps such as filtration.

In parallel, electrospinning offers a straightforward route to fabricate nanofibrous mats (NF-mats) with high specific surface area, interconnected porosity, and tunable surface chemistry, and can be implemented with relatively low start-up costs at the laboratory scale [14–16]. While scalable electrospinning configurations, such as multi-jet and needleless setups and continuous collection, have been explored to increase productivity [17, 18], practical implementation may still be constrained by throughput, sensitivity to solution and ambient conditions, and solvent/energy demands [19, 20]. Importantly, electrospun mats enable immobilization of active components into a robust, retrievable architecture, maximizing the liquid-solid interfacial area while eliminating particle dispersion and post-processing filtration. Accordingly, an electrospun, reusable catalytic mat may offer a practical route toward filtration-free CEC, addressing implementation challenges commonly associated with particulate CEC systems.

In this study, to address these challenges, a novel electrospun nanocomposite nanofibrous mat (NF-mat) composed of SiO_2 and PVDF is developed, where the SiO_2 is incorporated into an electrospun PVDF backbone to modulate interfacial properties and enable enhanced CEC under ultrasonication. The electrospun nanofibrous architecture affords a high specific surface area and roughness, significantly increasing the availability of an effective LS-CE interface for ultrasonication-assisted CEC. This, in turn, promotes interfacial charge transfer and ROS generation. Crucially, by immobilizing the PVDF and SiO_2 components within

the fibrous matrix, the proposed NF-mat obviates the need for catalyst pre-dispersion or post-reaction filtration. This design simplifies operation while effectively mitigating concerns regarding catalyst loss and secondary contamination. By virtue of its mechanical robustness, the NF-mat maintains structural integrity under continuous ultrasonic agitation and can be readily recovered and reused via simple rinsing. Consequently, the NF-mat enables the effective decolorization of both cationic (methylene blue, MB) and anionic (methyl orange, MO) dyes while retaining high efficiency over multiple cycles, demonstrating a practical CEC platform with broader potential applicability for environmental remediation.

2 Materials and methods

2.1 Fabrication of SiO_2-PVDF NF-mat

Silicon dioxide (SiO_2, Extra Pure grade, 99.0% purity, quartz) was purchased from Kanto Chemical Co., Inc. Poly (vinylidene fluoride) (PVDF; Sigma Aldrich, 182702; Molecular weight (M_w)≈534,000 g/mol), acetone, and N-dimethylformamide (DMF) were purchased from Sigma Aldrich. For the preparation of the PVDF nanofibrous mat, 20 wt% of PVDF and 9.6 wt% of SiO_2 are mixed with the solvent, which is composed of DMF/acetone mixed to a ratio of 7:3. Initially, the measured mass of PVDF powder was added gradually to the solvent and stirred continuously. Subsequently, the SiO_2 particles were added to the PVDF solution and stirred for 6–8 h at 55–60 °C to thoroughly mix them to make a homogenized solution. During stirring, the solution was monitored by visual inspection for any phase separation or particle settling, and no visible separation or sedimentation was observed. To fabricate a nanofibrous mat, the electrospinning machine (ES 100, NanoNC, Republic of Korea) was employed, and the prepared solution was poured into a syringe having a needle gauge of 19 and then fitted into the electrospinning machine. The flow rate was adjusted from 1.5 to 2.0 mL/h, and a high-voltage supply (HV30N, NanoNC, Republic of Korea) was used to provide a negative driving voltage around −17 kV. During the electrospinning process, the tip-to-collector distance was set to approximately 15 cm. The central electrospun region is collected for the NF-mat for the fiber structure uniformity. Following electrospinning, the manufactured NF-mat was put into the oven at approximately 60–70 °C overnight to eliminate the residual solvents and to maintain the structural integrity. Moreover, the thin-film (TF) was also fabricated with the same composition of 20 wt% of PVDF and 9.6 wt% of SiO_2; then it was dried in an oven under identical conditions as applied to the NF-mat. Furthermore, to study the influence of SiO_2 on the performance of NF-mat, three different concentrations of SiO_2 were added to fabricate the nanofibrous mats while keeping the amount of PVDF fixed (i.e., 20%). Three different concentrations of SiO_2 are as follows: 3.2 wt%, 6.4 wt%, 9.6 wt%. These three variations provided a systematic insight into how SiO_2 concentration behaved over the decolorization or removal of both dyes.

2.2 Decolorization of the dye

The ultrasonic bath cleaner (480 W, 40 kHz, DH.WUC. D06H, Daihan Scientific Co. Ltd, Republic of Korea) was prepared for CEC. Methyl orange and methylene blue dyes were bought from Sigma Aldrich. The 130 mg of prepared NF-mat was immersed in the 5 ppm aliquots (10 mL) of MB and MO dye solutions and then put under constant ultrasonication. The ultrasonic treatment time for MB and MO for complete removal was recorded as up to 4 h and 8 h, respectively. The recyclability of the NF-mat was evaluated by subjecting it to the newly prepared dye solutions multiple times. The operational structural stability of the NF-mat was systematically assessed by recycling it 9 times for MB and 7 times for MO. After each cycle, the NF-matrices were thoroughly rinsed with DI water, oven dried, and reintroduced to the fresh dye solutions.

2.3 Characterization of the dye decolorization

UV-visible spectroscopy was employed to evaluate the removal efficiency of MB and MO under ultrasonic treatment. Before the decolorization experiments, the absorbance spectra of 5 ppm stock solutions were recorded using a UV-visible spectrometer (V-650, Jasco, USA) across the respective wavelength ranges. After immersing the NF-mat, the decrement was observed at the characteristic absorption peak (λ_{max}) of the treated dyes after each hour of ultrasonication. The controlled experiments were also conducted under identical experimental conditions to isolate the contribution of NF-mat in dye removal. The removal or decolorization efficiency was calculated by monitoring the decrease in their absorbance spectra at the respective λ_{max} (664 nm for MB and 464 nm for MO) by using the following Eq. 1).

$$RE = \frac{(A_0 - A_t)}{A_0} * 100 \quad (1)$$

Where A_0 and A_t are initial and time-dependent absorbance values.

2.4 Chemicals used for capturing the ROS

Different chemicals were used to quench or scavenge the ROS, specifically OH and $O_2^{\cdot-}$. The following chemicals were used to confirm ROS. Isopropyl alcohol (IPA) and water-soluble tetrazolium salt-1 (WST-1) were bought from Sigma Aldrich, and superoxide dismutase (SOD) was purchased from ThermoFisher Scientific. Six solutions of equal volume of both dyes, containing NF-mat, were prepared to quench the ROS, i.e., two solutions for OH for MB and MO, and in the same way, two solutions for $O_2^{\cdot-}$ and two for the comparative study. These chemicals were added to the four dye solutions, in which two of them were of MB, i.e., one MB solution contained ROS quencher, and the other MB solution was without ROS quencher. Similarly, it was performed for MO solutions. IPA is utilized to quench the OH species from both MB and MO, and WST-1 and SOD were used to quench the $O_2^{\cdot-}$ for MB and MO, respectively.

3 Results and Discussion

3.1 Overall schematic and performance comparison of NF-mat

Figure 1 demonstrates a comprehensive overview of the novel synthesized NF-mat's fabrication process, functional implementation, and recyclability. As depicted in Fig. 1a**)**, the NF-mat is fabricated for the decolorization of the synthetic charged dyes, where the ultrasonication is utilized as a mechanical stimulus for continuous CE. The electrospun NF-mat is employed due to its enhanced surface area, increased hydrophobicity, and moderate roughness, as mentioned in previous studies, which shows the largest surface area of the PVDF in the nanofibrous form compared to its other forms [1]. The quartz form of SiO_2 is employed with its high stability and wear resistance, so that the particle integrity can be maintained under repeated ultrasonication [21]. Also, the PVDF with M_w of 534,000 is employed for the sufficient chain entanglement and viscoelasticity, which are important for stable electrospinning and continuous fiber formation [22]. Consequently, the SiO_2-PVDF based NF-mat provides an increased effective LS-CE interface through its enlarged surface area, high hydrophobicity, and moderate roughness, which leads to an improved LS-CE rate, resulting in higher ROS generation to decolorize the dyes. This NF-mat is immersed in the dye solution, and the application of ultrasonic energy induces dye decolorization. Significantly, the fabricated NF-mat has been recycled multiple times for both synthetic dyes, which underscores its reusability, structural integrity, and catalytic compatibility to decolorize both cationic and anionic dyes. Figure 1b**)** presents the optical image of the NF-mat, which is fabricated with the electrospinning process, and Fig. 1c**)** illustrates the scanning electron microscopy (SEM) image of the NF-mat; the morphology reveals the robust and uniform bonding between SiO_2 and PVDF particles as a nanofibrous matrix. In Fig. S1a**)**, the SEM image and average diameter analysis of the six random points from the fabricated NF-mat are demonstrated to verify the uniform and reproducible structure. As shown in Fig. S1b), the mean fiber diameter is approximately 1.38 μm across six points, and no statistically significant differences can be observed among them. In this context, the uniformity of the NF-mat morphology can be demonstrated, reducing concerns about the reproducibility of CEC performance. Also, to further support the mechanical robustness, a stress-strain (S-S) curve is presented, showing the onset of failure at a strain of 0.031 mm/mm (at tensile stress of 0.68 MPa), as shown in Fig. S2. According to this graph, the Young's modulus of the NF-mat can be estimated to be 82.62 MPa by its calculation between the tensile strain range from 0.005 to 0.009 mm/mm. Considering these results, the NF-mat exhibits sufficient mechanical robustness for handling and recycling experiments. Figure 1d**)** demonstrates the elemental mapping of the NF-mat attained from the energy dispersive X-ray spectroscopy (EDS) analysis, which shows the homogeneous distribution of the Si, O, F, and C with the atomic weight% of 2.56%, 3.15%, 50.10%, and 44.19%, respectively. EDS analysis suggests that the SiO_2 particles are preferentially located at the fiber surface, since their average diameter (5.54 ± 1.44 μm; Fig. S3) exceeds the average fiber diameter [23]. Therefore, the particles are more likely to be surface-attached or partially embedded rather than fully encapsulated within the fiber core. To further supplement this interpretation, transmission electron microscopy (TEM) images are acquired to examine the SiO_2 dispersion state within the fiber, as shown in Fig. S4. The overall fiber morphology is shown in Fig. S4a). However, distinct lattice fringes are not clearly observed in the selected regions, as shown in Fig. S4b), and the corresponding Selected Area Electron Diffraction (SAED) pattern exhibited a diffuse halo rather than sharp diffraction rings, which is in accordance with the previous reported work for SiO_2 [24] as shown in Fig. S4c). These observations indicate predominantly amorphous or low crystallinity features in the probed areas. With this analysis, the morphology of the NF-mat and its chemical composition are well demonstrated. To show the effectiveness of the NF-mat, the contact angle (CA) of the SiO_2-PVDF thin film (TF) and NF-mat is demonstrated in Fig. 1e**)**. The TF exhibits a hydrophilic nature with a contact angle (CA) of 48.5°, whereas NF-mat exhibits hydrophobicity with a high contact angle of 142.2°. This hydrophobicity can suppress liquid spreading and promote discrete droplet contact, thereby increasing the

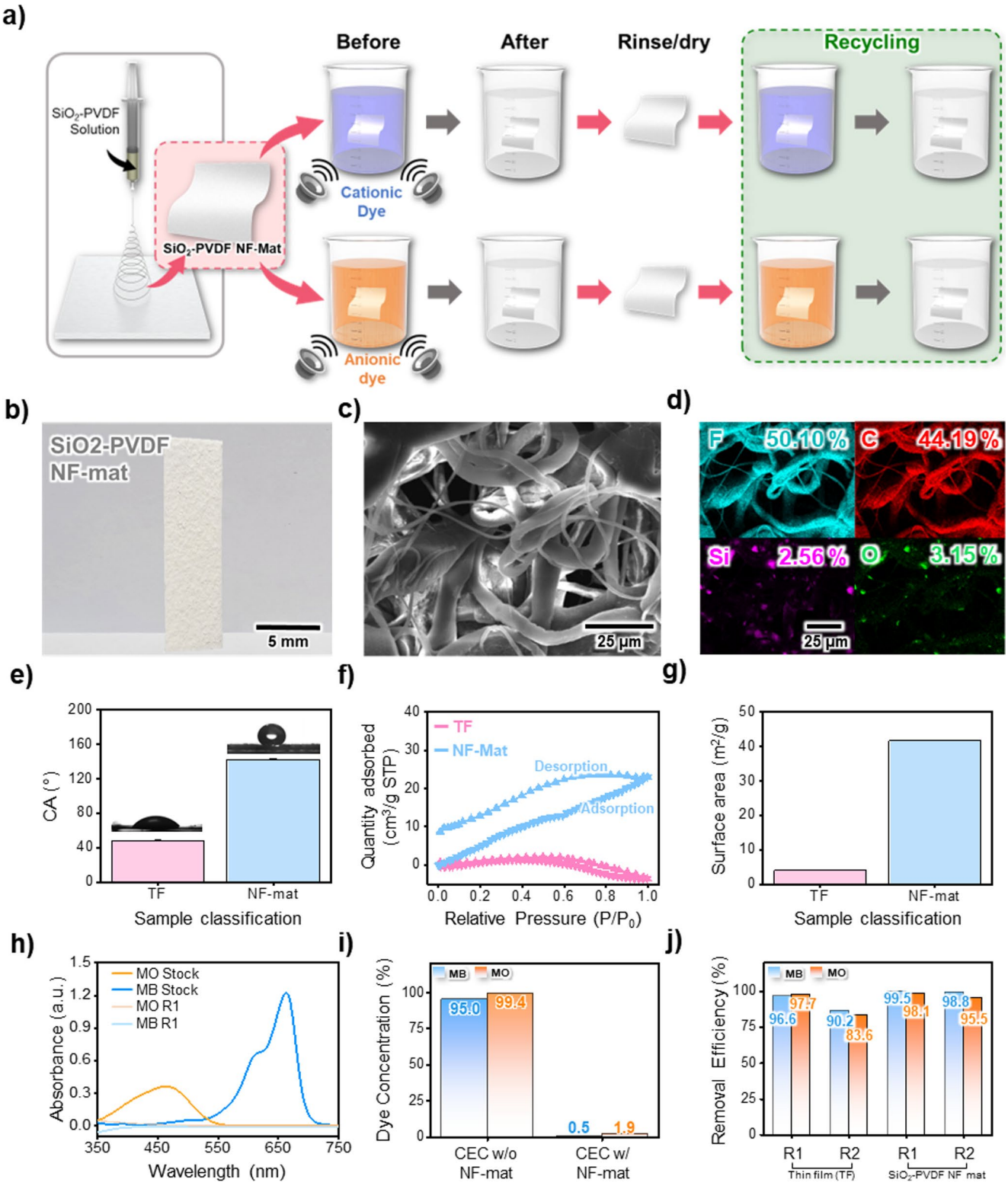

Fig. 1 **a)** A schematic of the overall experimental process. **b**, **c)** The optical and SEM images of SiO_2-PVDF NF-mat before treatment, and **d)** energy dispersive spectroscopy (EDS) image of the untreated NF-mat. **e)** Contact angle comparison between NF-mat and its TF counterpart. **f)** BET adsorption–desorption analysis of NF-mat and TF, and calculated **g)** surface area of NF-mat and TF based on BET characterization. **h)** UV-visible spectroscopy comparison between MB stock and MB after treatment, and MO stock and MO after treatment. **i)** Comparison between with and without NF-mat after treatment with respect to remaining dye concentration %. **j)** The removal efficiency comparison of NF-mat and TF for MB and MO

effective LS-CE interface, particularly near the three-phase contact line where repeated contact-separation events can occur under ultrasonication. According to previous reports [24], LS-CE on surfaces approaching superhydrophobicity can favor electron-dominated charge transfer rather than ion transfer. Therefore, the increased hydrophobicity of the NF-mat is expected to promote electron transfer. This enhanced interfacial activity may increase the generation of ROS, resulting in an accelerated decolorization. Figures 1f**)** and 1g) describe the textural properties of the NF-mat and a TF by performing nitrogen (N_2) adsorption-desorption analysis using the Brunauer-Emmett-Teller (BET) technique. The NF-mat demonstrates a characteristic mesoporous N_2 adsorption–desorption isotherm of type IV [25] with a hysteresis loop depicting a high N_2 adsorption capacity. This outcome reveals a higher surface area and enhanced porosity of NF-mat. The TF, on the other hand, exhibited a very low N_2 uptake, which can be attributed to its lower surface area, higher density, and poorer porosity than NF-mat. The NF-mat has a significantly greater BET specific surface area and t-plot micropore volume (41.6 m^2/g and 0.02 cm^3/g) compared to the thin film (4.1 m^2/g and 1.3×10^{-4} cm^3/g). Both materials fall into the small-mesopore boundary with average pore sizes of around 3.2 nm for the nanofibrous mat and about 2.0 nm for the thin film, as determined by BET (4 V/A) [26], summarized in Table 1. These findings verify that compared to the dense thin film, the electrospun nanofibrous architecture offers a much more open and hierarchically porous network, providing a significantly larger accessible surface and pore space that is beneficial for the targeted LS-CE process.

Figure 1h**)** demonstrates the UV-visible spectra of stock and ultrasonically treated solutions of MO and MB dyes. After the ultrasonic treatment on both dye solutions, the flattening of the absorption peaks is observed, which is evidence of a significant decolorization of the dye contents in the contaminated solutions by CEC. Figure 1i**)** highlights the remaining dye concentration % after the first cycle of ultrasonication for both controlled (without NF-mat) and experimental (with NF-mat) dye solutions. The remaining dye concentration is calculated by the absorption value of the fingerprint wavelength of each dye, which can be defined as the wavelength where the largest absorption peak occurs. The absorption data on the wavelength of 664 nm is used for the remaining MB concentration, while the absorption data on the wavelength of 464 nm is used for the remaining MO concentration. After completing the first cycle of the ultrasonic process, the MB and MO solutions without NF-mat represented a high percentage of remaining dye concentration, with residual dye concentrations up to 95% and 99.4%, respectively. On the other hand, the dye solutions containing NF-mat exhibited a lower dye concentration percentage, 0.5% for MB and 1.9% for MO, respectively, which verifies that the dye decolorization can result from a catalytic reaction between the NF-mat and dye solution. To evaluate the SiO_2 contribution to the dye decolorization, the removal efficiency of a PVDF-only NF-mat (without SiO_2) is compared with that of the SiO_2–PVDF NF-mat in Figs. S5a) to S5d)**.** For MB, the PVDF-only NF-mat achieved 52.6% removal after the first cycle, while the SiO_2–PVDF NF-mat reached 99.5% under identical conditions (Fig. S5b). Similarly, for MO, the PVDF-only NF-mat achieved 48.1% removal after the first cycle, whereas the SiO_2–PVDF NF-mat reached 98.1% (Fig. S5c)**.** These results indicate that SiO_2 incorporation is associated with markedly improved removal efficiency, consistent with SiO_2-induced interfacial property changes that can facilitate LS-CE-related charge transfer and ROS-mediated oxidation. Figure 1j**)** demonstrates the performance comparison for CEC between TF and NF-mat under repeated cycles. The removal efficiency of TF appears to decrease immediately after the second recycling cycle of TF for both dyes, whereas the NF-mat exhibits stable performance after the second cycle for both dyes. These findings underscore the better performance and potential of NF-mat over TF as a reusable and highly effective methodology for both cationic and anionic dyes. Moreover, the prepared NF-mat is recycled for further recycling cycles, which will be discussed in later sections. In this context, the superiority of the NF-mat to the CEC-based dye decolorization can be demonstrated. For further comparative studies, the pristine FEP film is utilized under identical experimental conditions along with the reported NF-mat. The FEP film revealed consistently lower removal efficiency than the NF-mat over two consecutive cycles: 90.7% and 49.2% for MB and 95.6% and 52.7% for MO, compared with 99.5% and 98.8% for MB and 98.1% and 95.5% for MO for the NF-mat (Fig. S6). These outcomes validate the superior performance of CEC-driven NF-mat in terms of dye decolorization and reusability compared to the pristine FEP film.

Furthermore, we also compared the performance of NF-mat with that of other previously reported CEC-compatible materials, as outlined in Table 2. By systematically summarizing the constituent materials, the working mechanism, the requirement (or absence) of post-treatment filtration, mechanical stimulation, target dye types, and corresponding removal efficiencies, this table enables an objective assessment of the relative performance and operational

Table 1 BET and t-plot analysis of SiO_2-PVDF NF-mat and TF

CEC Material	BET surface area (m^2/g)	t-plot micropore Volume (cm^3/g)	Average pore diameter (nm)
NF-mat (SiO_2–PVDF)	41.6	0.02	~3.0–3.4
TF (SiO_2–PVDF)	4.1	1.3×10^{-4}	~2.0–2.2

Table 2 The comparison of electrocatalysts, mechanism, dye's nature, and electrocatalytic activity

CEC Material	Filtration	Mechanical Stimuli	Catalytic Mechanism	Dye's Nature	Catalytic Activity	Ref.
FEP/ICP Film	Not Req.	Ultrasonication	Electron transfer	5 ppm: anionic	~90%, 300 min	[27]
TiO_2 NPs	Required	Stirring	Electronic transition and electron transfer	20 mgL^{-1} : cationic	~93.1%, 250 min	[28]
FEP powders	Required	Ultrasonication	Electron transfer	5 ppm: anionic	~98.1%, 180 min	[10]
$BaSrTiO_3$ NPs	Required	Stirring	Electronic transition and electron transfer	5 ppm: cationic	~99.0%, 180 min	[29]
PTFE	Required	Grinding	Electron transfer	5 ppm: anionic	~99.2%, 120 min	[30]
SiO_2 -PVDF NF-mat	Not Req.	Ultrasonication	Electron transfer (MB, MO); concurrent MB adsorption	5 ppm: cationic and anionic	MB:~99.5%, 240 min. MO:~98.1%, 480 min	This Work

characteristics of each system. The comparative analysis indicates that the prepared NF-mat achieved efficient decolorization of both cationic and anionic dyes via ultrasonication-induced LS-CE. Collectively, these results proposed that NF-mat exhibits a favorable combination of operational simplicity, broader dye compatibility, and competitive decolorization performance, thereby underscoring its technological distinctiveness within the current state of the art.

3.2 Characterizations of NF-mat before and after contact-electro-catalysis

Optical and morphological characterizations of NF-mat after the CEC are illustrated in Figs. 2a**)** and 2b**).** After the CEC treatment of the MB dye solution with NF-mat, the coloration of the NF-mat in blue is shown in the photograph **(**Fig. 2a**)**-i) and MB dye particle lump between the fibers shown in the SEM image **(**Fig. 2a**)-ii)** are shown, which demonstrates the adsorption of the MB dye on the NF-mat from the CEC process. It can result from the electrostatic attraction that exists between the MB dye and the NF-mat for certain reasons. Firstly, as the negative electric field is applied during the electrospinning process and the electron is transferred from the water molecule to the NF-mat, and secondly, the LS-CE during the CEC process, subsequently, the NF-mat surface could attain a negative charge due to these phenomena. Therefore, the attractive Coulombic force would be responsible for attracting the cationic MB dye towards the negatively charged surface of the NF-mat [31]; thus, the removal of MB occurs through both physical adsorption and CEC. Figure 2b**)** demonstrates the photograph and SEM image of NF-mat, after the CEC treatment of the MO dye solution. Aside from NF-mat CEC treated under MO dye solution, neither obvious coloration nor morphology modifications in the NF-mat can be observed, as shown in Figs. 2b)-i and 2b)-ii, which verifies that the removal of MO is dominated by the decolorization process via CEC rather than the adsorption mechanism. For the detailed demonstration, Fourier transform infrared (FT-IR) spectra of NF-mat before and after the CEC treatment for both dyes are shown in Fig. 2c**).** The blue line graph defines the FT-IR of the MB-treated NF-mat, which revealed that the stretching vibration bands corresponding to the $C_{het}{=}N^{+}(CH_3)_2$ bonds for MB can be found at 1648 cm^{-1} [32]. The localization of the intensive stretching vibrations of C = C and C-N can be found at 1600 cm^{-1} [32, 33]. Moreover, the stretching vibration of the C-C and C-N bonds of the heterocycle is localized at 1540 m^{-1} [34]. These results may correspond to the adsorption of the MB dye onto the mat surface according to the previously reported studies [32, 35, 36], which is also consistent with the previous SEM image Fig. 2a**)-ii**. On the other hand, the orange line represents the FT-IR spectrum of MO-treated NF-mat, which lacks characteristic bands of MO. Although a weak C-N stretching feature is observed at 1250 cm^{-1}, this signal alone does not provide clear evidence for appreciable MO adsorption on the NF-mat surface. To supplement this, the X-ray photoelectron spectroscopy (XPS) analysis is employed to validate the surface chemical transformations on the NF-mat before treatment (dull-black line) and after treatment with MB (blue line) and MO (orange line), as illustrated in Fig. 2d**).** These XPS spectra are deconvoluted and represented in Figs. 2e**)** to 2 g), which are signified mainly for MB and MO-related elements such as N1s, S2p, Cl2p, and Na1s. The topmost row of Figs. 2e**)** to 2g) illustrate the spectra of untreated NF-mat, which revealed mainly noise-level signals in the N1s, S2p, Cl2p, and Na1s regions. Moreover, the survey-based peak area of these elements is observed as 439, 200, 176, and 844 $CPS \cdot eV$, respectively, indicating the noise level signals that do not contribute to the meaningful contributions of elements [37]. However, following exposure to MB, as shown in the middle row of deconvoluted peaks, an N1s peak emerged around 399–400 eV [38] with a high peak area of 14404 $CPS \cdot eV$, thereby confirming the existence of nitrogen-containing MB residues or chemical intermediates on the NF-mat [39, 40].

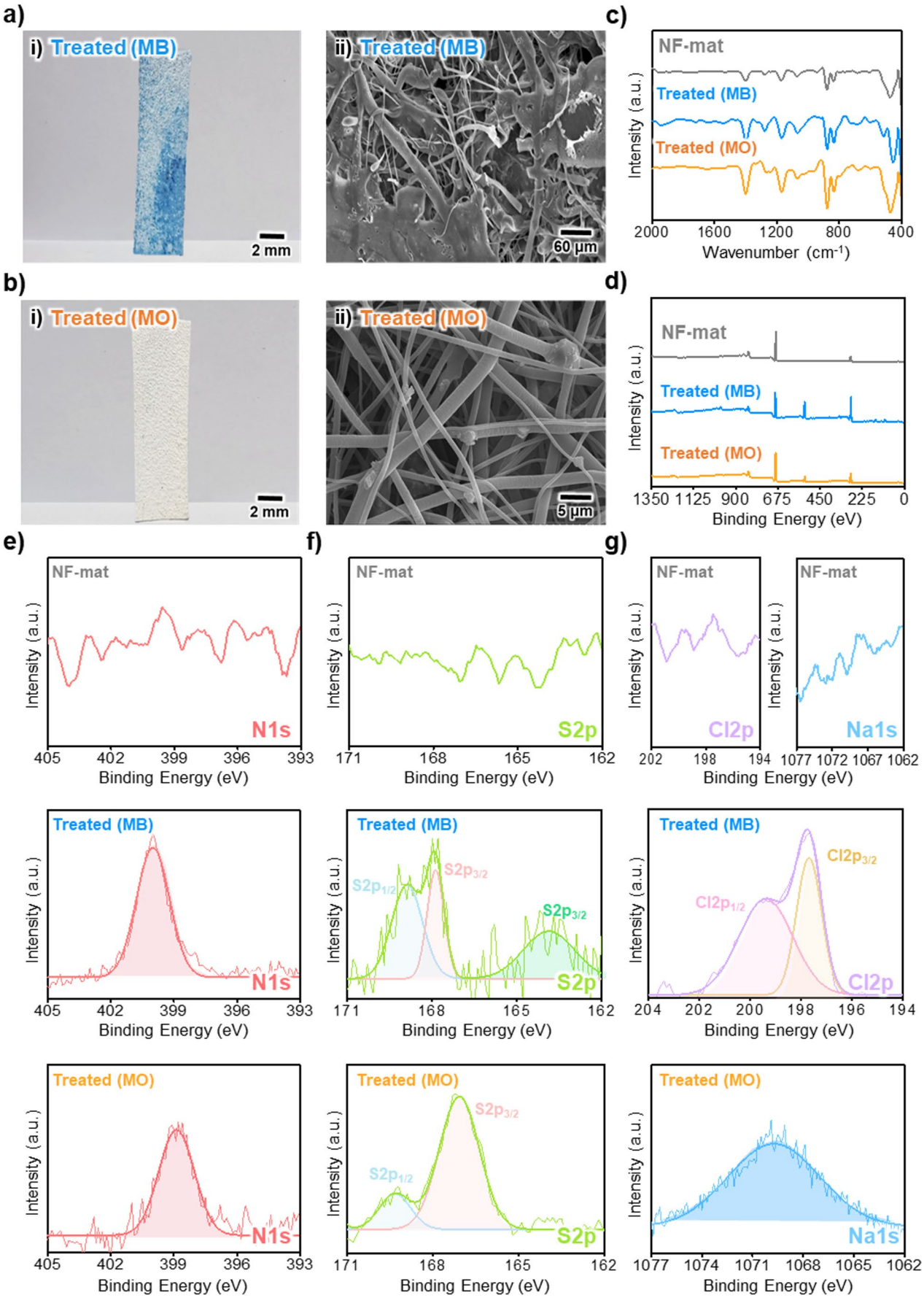
a)
i) Treated (MB)
2 mm
ii) Treated (MB)
60 µm
b)
i) Treated (MO)
2 mm
ii) Treated (MO)
5 µm
c)
NF-mat
Treated (MB)
Treated (MO)
Intensity (a.u.)
2000 1600 1200 800 400
Wavenumber (cm-1)
d)
NF-mat
Treated (MB)
Treated (MO)
Intensity (a.u.)
1350 1125 900 675 450 225 0
Binding Energy (eV)
e)
NF-mat
N1s
405 402 399 396 393
Binding Energy (eV)
f)
NF-mat
S2p
171 168 165 162
Binding Energy (eV)
g)
NF-mat
Cl2p
202 198 194
Binding Energy (eV)
NF-mat
Na1s
1077 1072 1067 1062
Binding Energy (eV)
Treated (MB)
N1s
Treated (MB)
S2p1/2
S2p3/2
S2p3/2
S2p
Treated (MB)
Cl2p3/2
Cl2p1/2
Cl2p
204 202 200 198 196 194
Binding Energy (eV)
Treated (MO)
N1s
Treated (MO)
S2p3/2
S2p1/2
S2p
Treated (MO)
Na1s
1077 1074 1071 1068 1065 1062
Binding Energy (eV)

Fig. 2 Characterization of NF-mat before and after the treatment. **a-i)** The optical and **b-ii)** SEM images of MB treated NF-mat, and **b-i)** optical and **b-ii)** SEM images of MO-treated NF-mat. **c)** The FT-IR spectra and **d)** high-resolution XPS survey spectra of untreated, MB-treated, and MO-treated NF-mats. **e-g)** The N1s, S2p, Cl2p, and Na1s regions for pristine NF-mat (first-row) and MB treated NF-mat (second-row), and the N1s, S2p, and Na1s regions for MO-treated NF-mat (last-row)

Additionally, high-resolution peaks for S2p, concentrated around 163.9 eV ($S2p_{3/2}$) corresponding to the C-S-C group, and at 167.9 eV ($S2p_{3/2}$) and 168.8 eV ($S2p_{1/2}$), are assigned to the sulfonate groups [40]. Moreover, the chlorine Cl2p doublet ($Cl2p_{1/2}$ and $Cl2p_{3/2}$) is detected around 199.4 eV and 197.7 eV, which likely originated from leftover chloride ions connected to MB. These findings suggest that a higher atomic concentration of MB-related elements on the NF-mat surface after ultrasonication. On the other hand, the deconvolution of high-resolution spectra of N1s, S2p, and Na1s for MO-treated NF-mat is illustrated in the last row of Figs. 2e**)** to 2g) [37]. The high-resolution spectrum of the N1s peak was found at 398.9 eV, and its peak area was found to be 5474 $CPS \cdot eV$. Moreover, S2p peaks focused around 167.1 eV and 169.3 eV ($S2p_{3/2}$ and $S2p_{1/2}$) as sulfonate groups. The Na1s peak appeared at 1069.7 eV, which may reflect the presence of limited MO-related surface residues on the NF-mat [27, 41]. The EDS elemental mapping also confirms the presence of these elements, as illustrated in Fig. S7. Taken together, these findings suggest that a limited amount of MO-related surface residues may remain on the NF-mat after treatment, rather than indicating appreciable MO adsorption. Accordingly, the removal of MO is considered to be predominantly governed by decolorization via the CEC process, which is consistent with the SEM observations showing negligible dye accumulation on the NF-mat. In contrast, the EDS elemental mapping showed the presence of MB-related elements (N, Cl, and S) distributed across the NF-mat surface [38, 39], as shown in Fig. S8. Consistent with the optical, FT-IR, and XPS results, these findings suggest more evident surface-associated MB residues on the MB-treated NF-mat. Overall, these results suggest that the adsorption contribution is more evident in the MB system, whereas MO removal is predominantly governed by decolorization via the CEC process, with only limited surface residues remaining after treatment.

3.3 Methodology and mechanism of decolorization process through Contact-electro-catalysis

The mechanism of the decolorization or removal of cationic and anionic dyes in the presence of the prepared NF-mat is proposed in Fig. 3. In the NF-mat, PVDF primarily serves as an electrospun fibrous backbone that provides a large accessible surface area and enables repeated LS-CE under ultrasonication. The incorporation of micron-scale SiO_2 (preferentially localized at/near the fiber surface) modulates the interfacial properties of the mat, including wettability and roughness, thereby increasing the effective LS-CE interface and facilitating interfacial charge transfer and ROS formation. This composite-specific interfacial modulation is consistent with the markedly improved removal performance of the SiO_2-PVDF NF-mat compared with PVDF-only NF-mat under identical conditions (Fig. S5). Especially, the overall phenomenon of interaction between a water (H_2O) molecule and NF-mat is demonstrated in Fig. 3a**).** The big red spheres represent the oxygen atoms, the white spheres represent hydrogen atoms, and the small black spheres denote electrons. As the ultrasound initiates, it stimulates the generation of cavitation bubbles (CBs) in the solution, as depicted in the red box. These tiny CBs encapsulate the dissolved gas (oxygen) and become large enough with time, and then implode after reaching their threshold size, as illustrated in the blue box. The implosion of CB creates high-pressure microjets that follow and interact with the water molecules adhered to the surface of NF-mat [42, 43], thus stimulating the contact-separation between water and NF-mat, which facilitates the electron (e^-) transfer between these two entities. In addition, hydrophobic surfaces can host interfacial nanobubbles. These nanobubbles may serve as cavitation nuclei under ultrasonication, locally enhancing microjet activity and interfacial renewal near the surface [44]. Although nanobubbles are not directly characterized in this study, their potential contribution is noted as a plausible factor that can enhance cavitation-assisted LS-CE at hydrophobic surfaces. Such localized cavitation can promote rapid attachment/detachment of the interfacial water layer from the NF-mat surface. Here, the term "contact–separation" is used to describe this repeated interfacial renewal of the liquid–solid interface between the interfacial water layer and the NF-mat surface under ultrasonication. This renewal promotes LS-CE-driven electron transfer and surface charging, while periodic separation helps mitigate rapid charge screening/relaxation in the liquid phase [45]. As a result, the NF-mat surface becomes negatively charged across a wide pH range as shown in Fig. S9, consistent with the general trend in LS-CE [46–48]. In addition, because PVDF is a piezoelectric material, ultrasonication-induced mechanical stress may generate polarization charges on the NF-mat, which potentially in principle, assist interfacial charge transfer and ROS formation. To evaluate this possible contribution, the piezoelectric coefficient (d_{33}) of the NF-mat is estimated as 0.80 ± 0.02 pC/N based on Fig. S10 in Supporting Information. Prior studies suggest that materials with such low d_{33} values are generally ineffective for piezocatalysis, indicating that the piezoelectric contribution is likely limited under this platform and that the observed activity is primarily governed by the CEC mechanism [49].

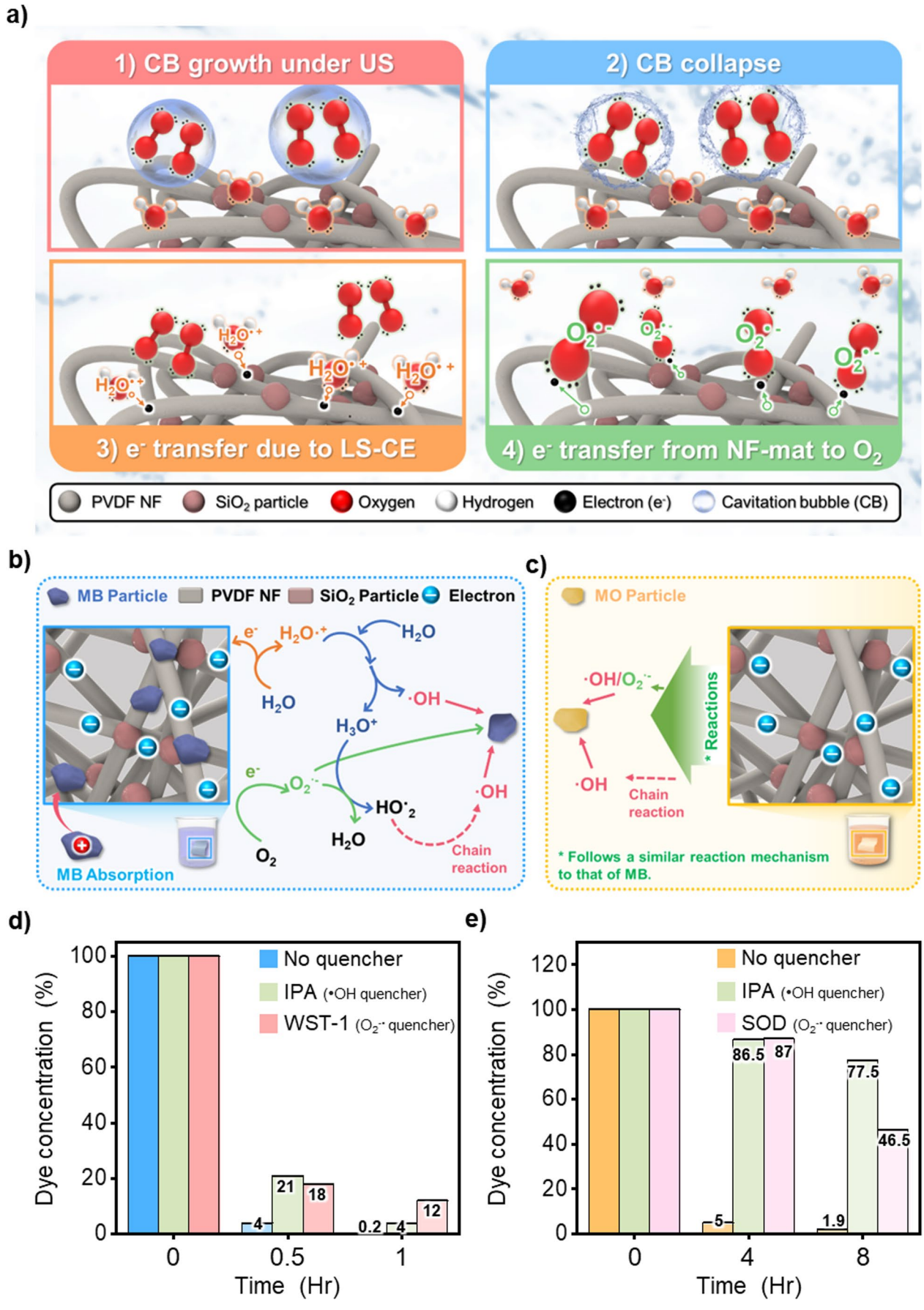
a)
1) CB growth under US
2) CB collapse
3) e⁻ transfer due to LS-CE
4) e⁻ transfer from NF-mat to O2
PVDF NF
SiO2 particle
Oxygen
Hydrogen
Electron (e⁻)
Cavitation bubble (CB)
b)
MB Particle
PVDF NF
SiO2 Particle
Electron
MB Absorption
Chain reaction
c)
MO Particle
* Reactions
Chain reaction
* Follows a similar reaction mechanism to that of MB.
d)
No quencher
IPA (•OH quencher)
WST-1 (O2•- quencher)
Dye concentration (%)
Time (Hr)
e)
No quencher
IPA (•OH quencher)
SOD (O2•- quencher)
Dye concentration (%)
Time (Hr)

Fig. 3 Operational mechanism of contact-electrocatalysis under ultrasonication. **(a)** Schematic representing the charge transfer phenomenon during ultrasonication. **(b)** The ROS generation and decolorization along with the adsorption of MB on NF-mat, and **(c)** the decolorization of MO via ROS in the presence of NF-mat. **(d)** CEC of MB dye with ROS quenchers, IPA for OH radicals, and WST-1 for O_2^- radicals, and **(e)** CEC of MO dye with ROS quenchers, IPA for OH radicals, and SOD for O_2^- radicals

Furthermore, the decolorization efficiency decreased monotonically with increasing ionic strength as shown in Fig. S11. This trend is consistent with LS-CE [50, 51], because dissolved ions can screen interfacial charges and enhance charge dissipation in solution, thereby suppressing LS-CE and the subsequent ROS generation. In contrast, a purely piezoelectric driven pathway is not expected to show such a strong dependence on ionic strength alone. Together with the low piezoelectric response of the NF-mat, the ionic strength dependence supports that CEC is predominant contribution in the dye decolorization. During this process, a water radical cation ($H_2O\cdot^+$) is generated, as depicted in the orange box [27]. Meanwhile, the O_2 released by the CB captures the electron upon encountering the pre-negatively charged surface of the NF-mat, and this interaction reduces the oxygen to superoxide radical ($O_2^{\cdot-}$) as portrayed in the green box [9, 10]. Building on these considerations about the ROS generation mechanism, the detailed dye decolorization process is shown in Fig. 3b**).**

As discussed previously, the electron transfer phenomenon assisted by LS-CE would be responsible for electron transfer from H_2O to NF-mat and responsible for the formation of water radical cation ($H_2O\cdot^+$), as follows:

$$H_2O + (SiO_2 - PVDF) \xrightarrow{ultrasound} H_2O^+ + (SiO_2 - PVDF)^- \quad (2)$$

Consequently, this water radical interacts with other water molecules and undergoes a proton transfer, which results in a hydroxyl radical ($\cdot OH$) and hydronium ion (H_3O^+) as stated in the following chemical reaction Eq. 3) [52].

$$H_2O^+ + H_2O \rightarrow \cdot OH + H_3O^+ \quad (3)$$

At the same time, the oxygen reacts with the NF-mat and receives the already existing electron from the surface of the NF-mat and is reduced to the superoxide radical ($O_2^{\cdot-}$) as illustrated in the following chemical reaction Eq. 4):

$$(SiO_2 - PVDF)^- + O_2 \; O_2^{\cdot-} + (SiO_2 - PVDF) \quad (4)$$

Following this, the superoxide radical ($O_2^{\cdot-}$) interacts with the hydronium ion (H_3O^+) and produces the hydroperoxyl radical ($HO_2\cdot$) as described in Eq. 5). The rest of the other superoxide radicals take part in the decolorization of dyes and convert them into unharmful products, as defined in Eq. 6) [53, 54].

$$O_2^{\cdot-} + H_3O^+ \rightarrow HO_2\cdot + H_2O \quad (5)$$

$$O_2^{\cdot-} + Dye \rightarrow Oxidized\ intermediates \rightarrow Mineralization\ products \quad (6)$$

As a result of successive chain reactions, the hydroxyl radical ($\cdot OH$) is generated, and it directly engages in the decolorization process of the MB dye [27]. Thus, the MB dye converts to harmless inorganic compounds, such as water (H_2O) and carbon dioxide (CO_2), as described in Eq. 7) [55].

$$.OH + MB \rightarrow Oxidized\ intermediates \rightarrow Mineralization\ products\ (CO_2 + H_2O + inorganic\ ions) \quad (7)$$

Along this process, the deposition of MB and the coloration of the NF-mat are also depicted in the bottom left corner of Fig. 3b**)**, in which MB (positive dye) gets attracted towards the negatively charged surface of NF-mat. Figure 3c**)** shows the decolorization mechanism of MO dye in the ultrasonic environment employing the identical NF-mat. Likewise, the removal of MO can also be attributed primarily to ROS generation through a mechanism similar to that discussed for MB. These ROS are considered to be mainly responsible for the breakdown of MO. This interpretation is consistent with the SEM and optical images (Fig. 2b**)**, which show no pronounced dye accumulation on the NF-mat. According to these outcomes, it is plausible to claim that NF-mat decolorizes the MO dye via ROS generation, which is described in Eq. 8) [56].

$$.OH + MO \rightarrow Oxidized\ intermediates \rightarrow Mineralized\ products\ (CO_2 + H_2O + inorganic\ ions) \quad (8)$$

As multiple reaction pathways and products are possible, the oxidation steps in Eq. 6) to 8) are presented schematically, where "oxidized intermediates" represents a mixture of transformation products rather than a single identified species.

Figures 3d**)** and 3e) **represent** the verification of ROS generation and their contribution to dye decolorization from the solution containing NF-mat. Figure 3d**)** shows the verification of specific ROS involved in the MB decolorization by applying ROS quencher, whereas the isopropyl alcohol (IPA) is utilized as an OH radical quencher, and WST-1 is

utilized as an $O_2^{\cdot-}$ radical quencher. During the ultrasonication for 1 h, both the IPA-added MB solution and the WST-1-added MB solution show suppressed dye decolorization behavior compared to the MB solution without quencher, which indicates that the CEC reaction is inhibited with the ROS quencher. This experimental result infers the ROS contribution to the MB decolorization, not only the MB adsorption towards the NF-mat. Similarly, Fig. 3e**)** demonstrates the verification of specific ROS involved in the MO decolorization by applying ROS quencher, whereas the IPA is utilized as an hydroxyl radical quencher, and superoxide dismutase (SOD) is utilized as an superoxide radical quencher. During the ultrasonication for 8 h, both the IPA-added MO solution and SOD added MO solution show suppressed dye decolorization behavior compared to the MO solution without a quencher, which also verifies that the dye decolorization primarily resulted from the ROS generation and its reaction with the dye. To probe the $\cdot$OH generation, terephthalic acid (TPA) is used as a fluorescent probe. Upon reaction with $\cdot$OH, TPA is converted to 2-hydroxyterephthalic acid, which exhibits a characteristic fluorescence peak at 425 nm. Figs. S12a) and S12b) shows the blank subtracted fluorescence spectra for the MB and MO dye, where a clear emission band in the 410–430 nm range is observed. Accordingly, the fluorescence intensity at ~420 nm is used as a semi-quantitative indicator of $\cdot$OH generation under the present conditions. For definitive identification and absolute quantification of radical species, future work will require electron paramagnetic resonance (EPR) measurements.

3.4 UV-Vis Spectroscopy of contaminated solutions before and after the treatment

The aliquots (3 ml) of cationic and anionic dyes (MB and MO) are characterized by UV-visible spectroscopy at specific intervals of time to inspect the decolorization efficiency after treating with and without the NF-mat under constant ultrasonication. Unless otherwise noted, an ultrasonication power of 480 W is applied, as higher power enhances the removal efficiencies of both dyes, which is demonstrated in Fig. S13. Figures 4a**)** to 4c) illustrates the UV-visible spectra for the MB solution; the red line in the graph represents the MB stock solution; the MB solution is treated for 4 h of ultrasonication, and the UV-visible spectra of the MB solution at each hour are demonstrated. This experimental result emphasizes the reduction in the characteristic absorption intensity at a specific wavelength of 664 nm. Subsequently, adding the NF-mat into the MB dye solution as the ultrasonic time increases, the absorption curve also becomes less steep and eventually flattens in 4 h. Figure 4b**)** shows the comparison between the controlled MB solution, i.e., the MB solution without NF-mat **(black dotted line)**, and the MB solution with NF-mat **(blue dotted line)**. The MB solution, which contains NF-mat, shows an impressive 4.6% remaining concentration of MB in the first hour. Finally, after 4 h of ultrasonication, the remaining concentration recedes up to 0.5%. On the contrary, the MB solution, which does not contain NF-mat, revealed 95.1% of the remaining concentration after four hours of constant ultrasonication, which clearly indicating that NF-mat removed the MB in the ultrasonically assisted environment. This experimental data is further verified with the time-lapse photos and Supplementary Video V1 of the MB stock solution and the treated MB solutions after each hour, as shown in Fig. 4c**)**, which shows the dye decolorization visually. To quantify the relative contributions of dye adsorption and ultrasonication-driven CEC, dark adsorption controls are performed under identical conditions (4 h stirring, same NF-mat mass, and solution volume) but without ultrasonication, with light excluded. As shown in Fig. S14a), adsorption alone resulted in an MB removal efficiency of 46.6%. Under ultrasonication-assisted operation, the MB removal increased to 99.5% (Fig. 4b), indicating an additional 52.9% removal beyond adsorption. This additional removal is attributed to ROS-mediated CEC decolorization rather than adsorption alone, supporting that CEC provides a major contribution under ultrasonication. To further characterize adsorption, a Langmuir adsorption isotherm analysis is conducted, as shown in Fig. S14b) and explained in Supporting Information. The adsorption parameters provide a semi-quantitative upper bound for adsorption-only uptake, and therefore adsorption alone cannot account for the near-complete MB removal observed under ultrasonication. These results collectively support that ROS-mediated CEC is the primary pathway for MB decolorization during ultrasonic operation.

Figures 4d**)** to 4f) show the decolorization behavior of MO. Figure 4d**)** presents the UV-visible spectra of the MO solution; the red line in the graph represents the MO stock solution, and the MO solution is treated for 8 h of ultrasonication, and UV-visible spectra of the MO solution are demonstrated every two hours. This experimental result emphasizes the reduction in the characteristic absorption intensity at a specific wavelength of 464 nm. As a result, a great decline in the characteristic absorption peak is observed in the first 4 h of treatment, and the peak is almost flattened after 8 h. Figure 4e**)** shows the remaining concentration % of MO in the solution and compares the results between two identical MO solutions, one containing NF-mat and the other without NF-mat. The MO solution, which contains NF-mat, shows an impressive 5% remaining concentration of MO in the first 4 h. After four more hours of ultrasonication, the remaining concentration decreases to 1.9%, while the MO solution without NF-mat shows negligible dye

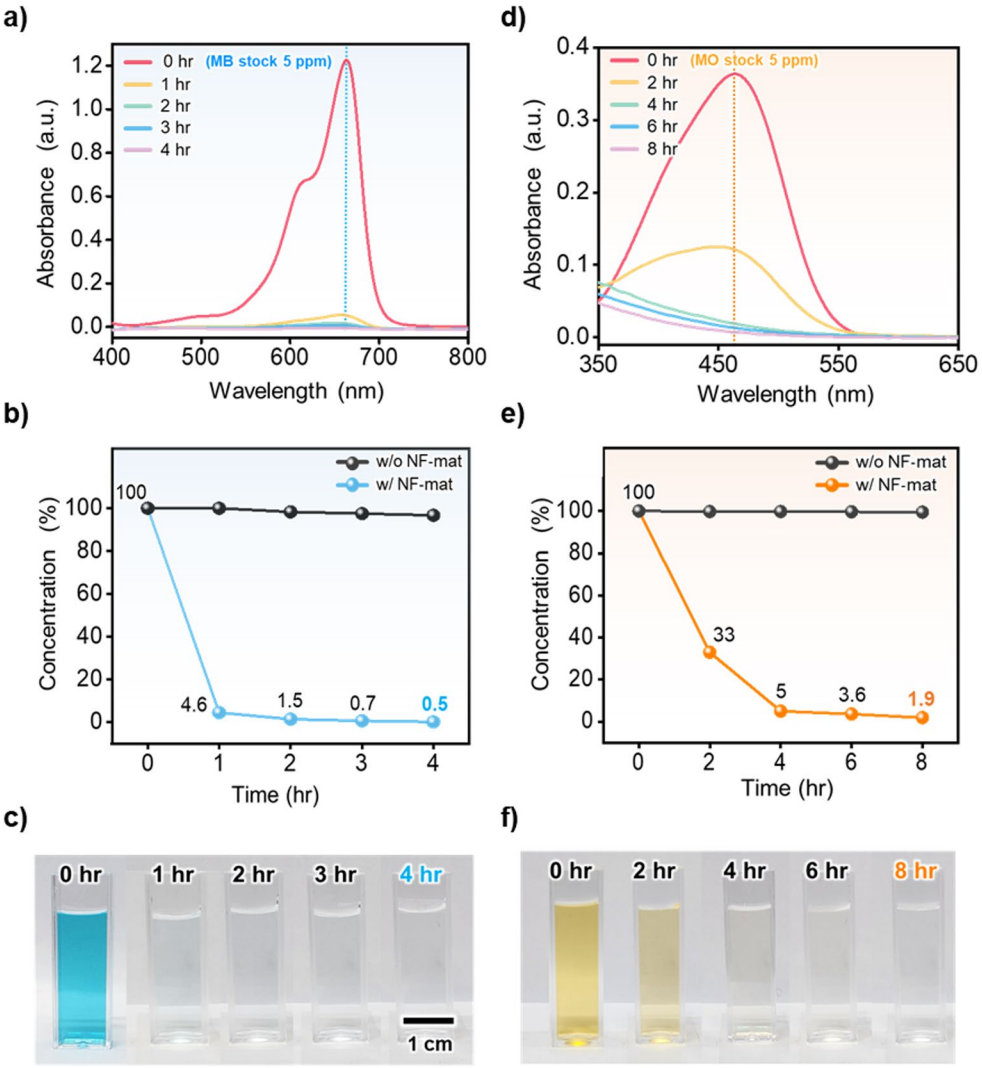

Fig. 4 Time-dependent dye decolorization behavior. **(a)** UV-visible spectra of MB during 4 h and **(b)** its remaining concentration % in the solution with and without the presence of NF-mat. **(c)** The timeline photos of the MB solution after each hour of ultrasonication. **(d)** UV-visible spectra of MO during 8 h, and **(e)** its remaining concentration % in the solution with and without NF-mat. **(f)** The timeline photos of the MO solution after 2 h of ultrasonication

decolorization even after 8 h of constant ultrasonication, which proves that the NF-mat effectively removed the MO in the ultrasonically assisted environment. As shown in Fig. 4f), this decolorization of MO can be visibly confirmed with time-lapse photos of the MO stock solution and Supplementary Video V2 and the treated MO solutions after every 2 h. To further examine the role of adsorption in the MO system, dark adsorption controls are also performed following the same procedure, except with 8 h stirring, as shown in Fig. S14c). In contrast to MB, MO shows no meaningful decrease in absorbance, indicating that the present data do not support an appreciable adsorption contribution in the MO system. Taken together, these results indicate that the prepared NF-mat can effectively treat both cationic and anionic dyes, while the adsorption contribution is more evident in the MB system and MO removal is predominantly governed by CEC-driven decolorization.

Considering the real wastewater contains mixed contaminants, inorganic salts, and suspended solids, the mixed dye (MD) solution containing rhodamine B (RhB), MO, MB, and crystal violet (CV) is applied to show the feasibility of the NF-mat application to the practical condition. Their visual photo and UV-visible spectra are shown in Fig. S15a). The UV-visible spectra during the MD solution decolorization are shown in Fig. S15b). To mimic the ion component in the real wastewater, NaCl is added at 0.1 M, and the UV-visible spectra during its decolorization are shown in Fig. S15c). Upon dye mixing, the characteristic absorption peak of the MD solution shifted to 554 nm; thus, the concentration change is monitored based on the absorbance peak at 554 nm, as shown in Fig. S15d). After 4 h of treatment, 0.5% of MB and 5.0% of MO remained, whereas the MD solution showed 8.8% remaining, indicating a reduced removal efficiency under MD conditions. After 8 h, the remaining concentration of the MD solution decreased to 4.8%, suggesting that further decolorization is achievable with extended treatment. Also, the MD solution containing 0.1 M NaCl exhibited stronger inhibition of dye decolorization: 20.0% of

MD remained after 4 h, and 7.9% remained after 8 h. These results indicate that both MD conditions and increased ionic strength can slow the decolorization kinetics. Accordingly, achieving a residual concentration below 1% for real wastewater is expected to require a longer treatment time than that of single-dye systems. Nevertheless, as decolorization continued with time, complete treatment of real wastewater appeared feasible with extended operation, which will be investigated in future work, including matrices containing suspended solids and representative inorganic ions. To further examine applicability beyond dyes, phenol (500 ppm) is tested as a representative phenolic/aromatic pollutant under the same conditions used for MB/MO. As shown in Fig. S16, phenol shows 11.5% removal after 7 h, based on the decrease of the characteristic UV–vis absorption band at ~260–270 nm. Although preliminary, this result suggests that the NF-mat-based platform can also treat non-dye aromatic organics with further optimization of the reactor configuration and ultrasonication parameters.

3.5 Decolorization kinetics

In Figs. 5a) to 5c), the pseudo-zero-, first-, and second-order kinetic models are applied to assess the decolorization kinetics of MB dye. The best kinetic model is determined by comparing the linear correlation coefficients (R^2) obtained from each fit, with the model exhibiting the highest R^2 value being selected as the best-fitting model. As depicted in Figs. 5a) and 5c) the pseudo-zero-order (PZO) and pseudo-second-order (PSO) kinetics revealed relatively low correlation coefficient (R^2 = 0.77 and R^2 = 0.67, respectively). In contrast, as represented in Fig. 5b), the linear fit of ln ($\frac{C_o}{C_t}$) vs. time as pseudo-first-order (PFO) kinetics yielded a good correlation coefficient (R^2 = 0.98), which is selected depending upon the best-fitting kinetic model among the other two models. Moreover, the apparent rate constant K_1 = 1.06 h^{-1} for first-order is observed. This model predicts that the reaction rate of MB decolorization is proportional to its instantaneous concentration (C_t) and can be written as following Eq. 9) [57, 58].

$$Reaction\ Rate = -dC/dt = K_1 C \tag{9}$$

where C_t is the MB concentration at time t, and K_1 is the pseudo-first-order rate constant. The linearized form is obtained by integrating this reaction rate in Eq. 10) as follows.

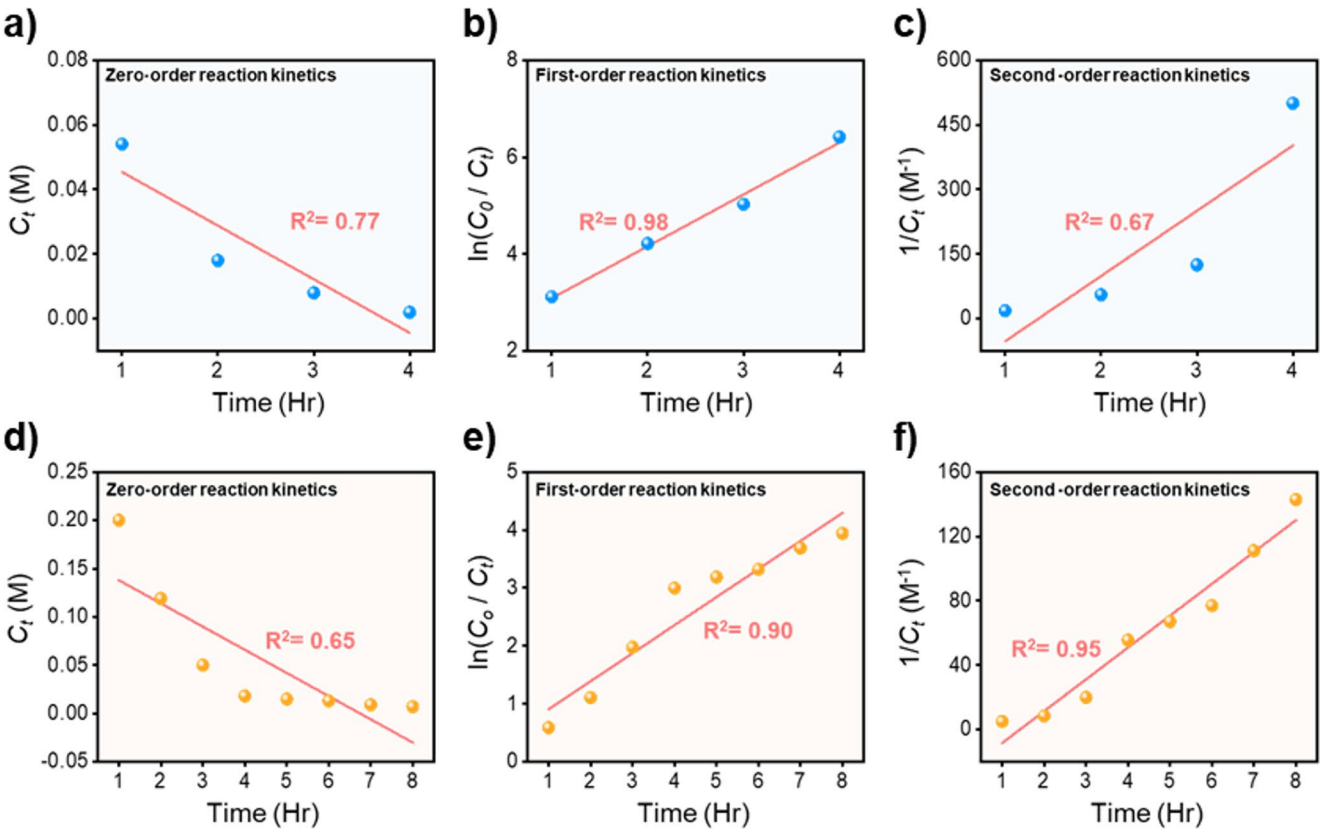

Fig. 5 Decolorization kinetics of MB and MO. **(a)** pseudo-zero, **(b)** pseudo-first, and **(c)** pseudo-second order kinetics for MB dye, and **(d)** pseudo-zero, **(e)** pseudo-first, and **(f)** pseudo-second order kinetics for MO dye

$$\ln\left(\frac{C_0}{C_t}\right) = K_1 t \tag{10}$$

where C_o is the initial MB concentration.

As a result, the pseudo-first-order kinetic behavior of MB suggests that the overall reaction rate is predominantly influenced by the MB concentration under the specified CEC–ultrasonication circumstances.

Similarly, as depicted in Figs. 5d) and 5e) the decolorization kinetics for MO are examined using pseudo-zero-, first-, and second-order kinetic models, and their R^2 values are 0.65, 0.90, and 0.95, respectively. Among these kinetic models, the pseudo-second-order (PSO) kinetic model is selected as a best fit by plotting $\frac{1}{C_t}$ against time, producing a straight line with a higher correlation coefficient value (R^2 = 0.95), suggesting that this model well describes MO deterioration. Under this assumption, the reaction rate is characterized by the effective bimolecular interactions between MO and ROS and can be written in terms of the MO concentrations C_t at time t as illustrated in the following Eq. 11) [59].

$$Reaction\ Rate = -\frac{dC}{dt} = K_2 C_t^2 \tag{11}$$

where K_2 is the pseudo-second-order rate constant, and C_t is the MO concentration at time t. Integration of the reaction rate equation provides the linearized form as following.

$$\frac{1}{C_t} = \frac{1}{C_0} + K_2 t \tag{12}$$

where the initial MO concentration is denoted by C_0. The slope of this plot revealed the apparent second-order rate constant, K_2 = 19.77 $ppm^{-1}h^{-1}$, using the same experimental conditions. Consequently, MO elimination adheres to pseudo-second-order kinetics, indicating a decolorization mechanism predominantly governed by bimolecular interactions between MO molecules and ROS in the bulk solution.

Based on the kinetic models, the electrical energy per order (E_{EO}, kWh/(m^3·order)), a widely used energy-based figure-of-merit for advanced oxidation processes (AOPs), is calculated [60]. Using the operating power, treatment time, and treated volume of the ultrasonication-driven CEC conditions employed in this study, the E_{EO} values are 83,000 kWh/(m^3·order) and 223,000 kWh/(m^3·order) for MB and MO, respectively, based on the measured decolorization endpoints. These absolute E_{EO} values are strongly affected by the small treated volume (10 mL in this study) and batch configuration, which inflate the kWh/m^3 normalization; thus, E_{EO} is primarily intended for within-study benchmarking and qualitative comparison. Compared with representative E_{EO} ranges reported for established AOPs, such as photo-Fenton (E_{EO} order of ~ 10^0 – 10^1 kWh/(m^3·order)), UV/catalyst (E_{EO} order of ~ 10^2 – 10^3 kWh/(m^3·order)), and ultrasound (E_{EO} order of ~ 10^3 – 10^4 kWh/(m^3·order)) [61], the E_{EO} values obtained in this study are higher. Because the E_{EO} depends on reactor configuration, treated volume, water matrix, and target compound, the cross-study comparisons should be interpreted cautiously. Importantly, comparison with previously reported CEC systems operated under similar laboratory-scale conditions indicates E_{EO} values of a similar order of magnitude [11, 62–64], as shown in Table 3, suggesting that reducing energy demand remains a key challenge for this emerging technology. Accordingly, future CEC research should focus on lowering E_{EO} by optimizing ultrasonication parameters and scaling up to increase treated volume per unit energy. Since CO_2e emissions scale with electricity consumption, such reductions in E_{EO} would proportionally reduce the carbon footprint, subject to region-specific grid emission factors. In parallel, the material versatility of CEC and the

Table 3 Comparison of E_{EO} values reported in previous CEC studies

CEC Material	Target	Operating Hour (Hr)	Ultrasonic Power (kW)	Volume (mL)	E_{EO} (kWh/(m³·order))	Ref.
PTFE	Antibiotics 1 mg/L	3	0.5	50	22,000	[64]
Etched FEP	MO dye 5 ppm	5	0.9	50	90,000	[27]
PTFE	Algae 1.76×10^6 cells/mL	5	0.24	120	25,000	[63]
Charged FEP	MO dye 5 ppm	4	0.6	50	24,000	[11]
NF-mat	**MB dye MO dye 5 ppm**	**4 (MB) 8 (MO)**	**0.48**	**10**	**83,000 (MB) 223,000 (MO)**	**This Work**

operational simplicity enabled by the immobilized NF-mat configuration motivate continued development toward practical applications.

3.6 Effect of increasing the SiO_2 content on hydrophobicity and surface area of NF-mat

For the deeper inspection of the NF-mat, three different NF-mats with distinct concentrations of SiO_2 while keeping the constant quantity of PVDF are fabricated to investigate the effect of SiO_2 on the removal of cationic and anionic dyes. Figure 6a**)** represents the UV-visible spectra of MB solutions that are treated under the NF-mats with three different SiO_2 compositions for **four hours** under continuous ultrasonication. As the SiO_2 concentration becomes higher from 3.2 wt% to 9.6 wt%, the UV-visible spectra in Fig. 6a**)** become flattened, which shows MB removal efficiency increment from 66.8% to 99.4%, as shown in Fig. 6b**).**

Figure 6c) illustrates the UV-visible spectra of three identical solutions of MO dyes, which are treated with three different SiO_2 concentrations of NF-mats. As expected, here as well, the NF-mat with 9.6 wt% SiO_2 showed the lowest characteristic absorbance curve for MO, indicating the highest removal efficiency compared to the other two concentrations (3.2 wt% and 6.4 wt%). As shown in Fig. 6d**)**, the NF-mat with a SiO_2 concentration of 9.6 wt% exhibits the highest decolorization efficacy of 98.1%, which is higher than the other two lower SiO_2 concentrations in the NF-mat.

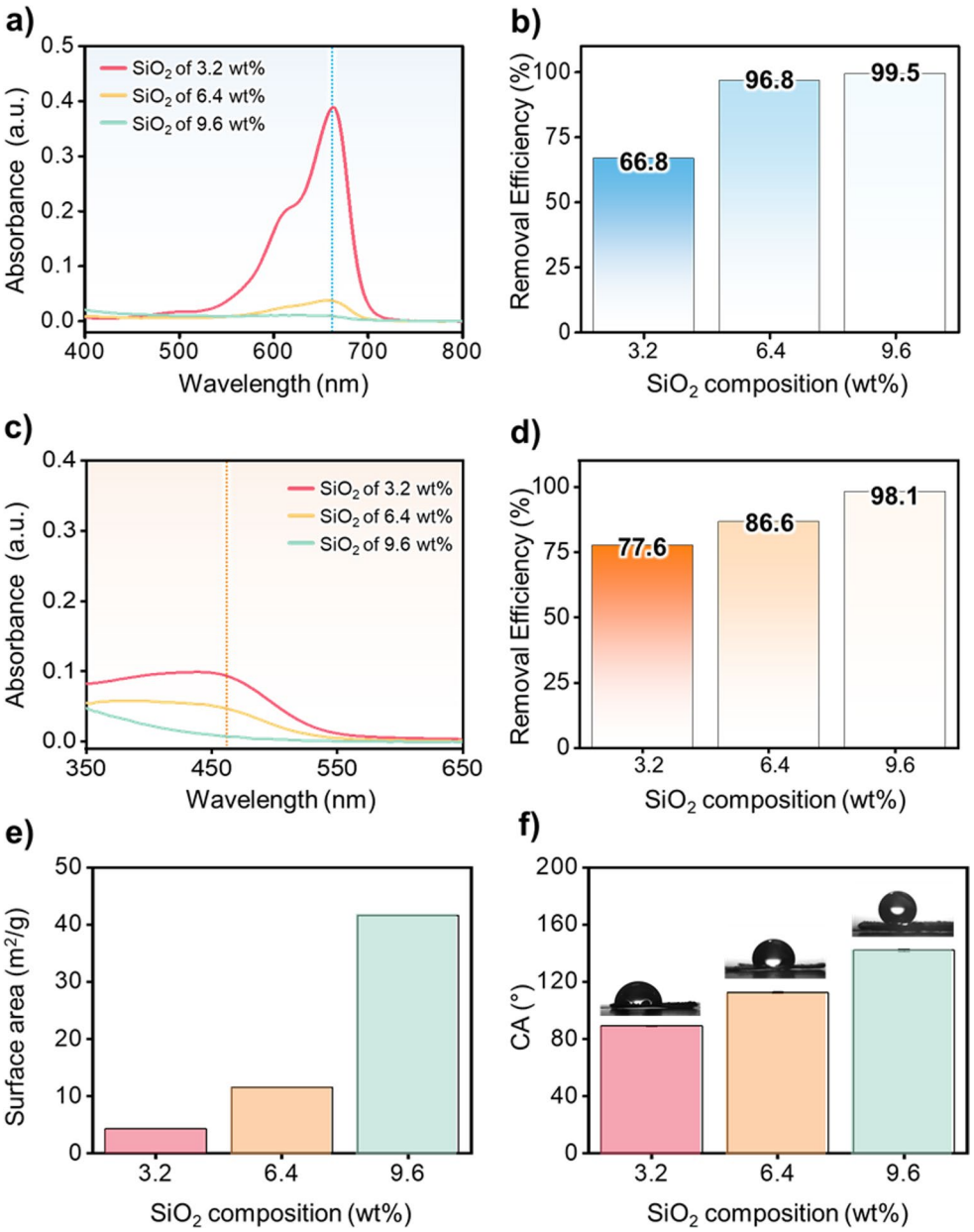

Fig. 6 Effect of different concentrations of SiO_2 under a fixed amount of PVDF in NF-mat. **(a)** UV-visible spectroscopy of three different concentrations of NF-mat treated for MB dye, **(b)** removal efficiencies for these three concentrations. **c-d)** UV-visible spectroscopy for MO dye NF-mats and their respective removal efficiencies. **e)** BET surface area comparison **f)** and contact angle comparison of various concentrations of SiO_2 in NF-mat

These quantitative analyses for MB and MO dyes revealed that the prepared NF-mat with a composition of 9.6 wt% of SiO_2 and 20 wt% of PVDF has a rich capability for the dye decolorization with a high-performance rate without discriminating the ionic nature of the dye.

To supplement these experimental results, the BET result of the NF-mat depending on the SiO_2 particle composition is shown as shown in Fig. 6e**)**, which shows a surface area increment from 4.28 m^2/g to 41.64 m^2/g with SiO_2 composition enhancement from 3.2 wt% to 9.6 wt%. This experimental result shows an increasing number of reaction sites with SiO_2 composition enhancement, which can be a dominant factor in the enhanced dye decolorization at higher SiO_2 composition. Also, to explore the wetting property changing resulting from the SiO_2 composition, which is one of the dominant factors on the LS-CE, the CA of each case is shown in Fig. 6f**).** As the SiO_2 composition enhanced from 3.2 wt% to 9.6 wt%, the CA also increased from 89.2 ± 0.5 ° to 142.2 ± 1.0 °.

As mentioned, in previous research [24] only the electrons are transferred during the LS-CE under a superhydrophobic surface, whereas both ion and electron transfer occur with LS-CE under hydrophobic and hydrophilic surfaces. As the electron transfer between the liquid and solid is directly attributed to the CEC, as mentioned in **Sect. 3.3**, the enhanced hydrophobicity resulting from the SiO_2 addition can be attributed to the enhancement of the dye decolorization ability, as well demonstrated in Fig. S17. Taken together, these results indicate that increasing the SiO_2 content simultaneously enlarges the accessible reaction sites through surface area increment and promotes electron-dominated LS-CE through increased hydrophobicity [65], both of which synergistically contribute to the superior CEC performance. On this basis, the NF-mat with 9.6 wt% of SiO_2 is selected as the optimal contact-electro-catalyst for subsequent experiments.

3.7 Recyclability comparison of SiO_2-PVDF NF-mat versus thin film

The superiority of the NF-mat with SiO_2 and PVDF contents of 9.6 wt% and 20 wt% for the contact-electro-catalyst for both cationic and anionic types of dyes is well demonstrated in previous sections. However, as well as the dye decolorization efficiency, the recyclability of the contact electrocatalyst must be considered for the application of the CEC technology in practice. In this context, both the MB and MO decolorization behaviors for multiple rounds after the rinsing and drying of the catalyst are demonstrated. For the detailed comparison, the UV-visible spectra of MB dye solutions treated in the first and second rounds of TF and NF-mat are shown in Fig. 7a**).** For the TF, MB dye decolorization under its second recycling cycle shows a significant decrease when compared to its first cycle, whereas the second cycle of NF-mat does not show a large decrement in the dye removal behavior. For the deeper inspection about the recyclability of the NF-mat for the MB decolorization, the MB removal efficiency under the several recycling rounds is shown in Fig. 7b**).** Although the fabricated NF-mat is recycled nine times, the removal efficiency of the MB is maintained over 95%, which demonstrates its superior recyclability even if the adsorption of the MB occurs simultaneously with the catalytic reaction. To further verify it, the UV-visible spectra of MB dye solutions treated in the second recycling cycle of TF and the ninth cycle of NF-mat are shown in Fig. 7c**)**, which shows that the NF-mat that underwent ninth recycling retains higher removal efficiency compared with TF that underwent second recycling. Furthermore, the UV-visible spectra of MO dye solutions treated in the first and second rounds of TF and NF-mat are shown in Fig. 7d**)**, which shows similar removal efficiency decolorization behavior with that of MB. To further verify the recyclability of the NF-mat, the MO removal efficiency under the seven recycling rounds is shown in Fig. 7e**)**, which shows that removal efficiency over 96% can be retained during each cycle. To emphasize its superior recyclability, the UV-visible spectra of MO dye solutions treated in the second recycling round of TF and seventh recycling round of NF-mat are shown in Fig. 7f), which indicates that the NF-mat that underwent seventh recycling retains a higher removal efficiency compared with TF that underwent second recycling.

Moreover, this recyclability is further demonstrated with post-cycling morphology assessment by SEM after repeated operation, as shown in Fig. S18a. The SEM image shows the fiber morphology of the NF-mat after the ninth recycling cycle of the MB (Fig. S18b) and after the seventh recycling cycle of the MO (Fig. S18c). After MB cycling, surface coverage consistent with dye adsorption is observed on the fibers, similar to the appearance on the MB-treated NF-mat shown in Fig. 2a**)-ii**. Importantly, the fibrous network remains intact without evidence of severe fiber breakage or collapse. For the MO-treated NF-mat, the fiber morphology is largely preserved with no noticeable deformation, consistent with Fig. 2b**)-ii**. With these SEM characterizations, it can demonstrate the structural integrity of the NF-mat even after multiple recycling rounds.

Despite the robust decolorization under the repeated rounds, secondary pollution arising from the release of fiber fragments or SiO_2 particles should be evaluated from an environmental perspective. Fig. S19 presents the NF-mat mass measured after each round as an indirect indicator of material loss; no measurable mass change was observed for either MB or MO, suggesting minimal macroscopic shedding. To

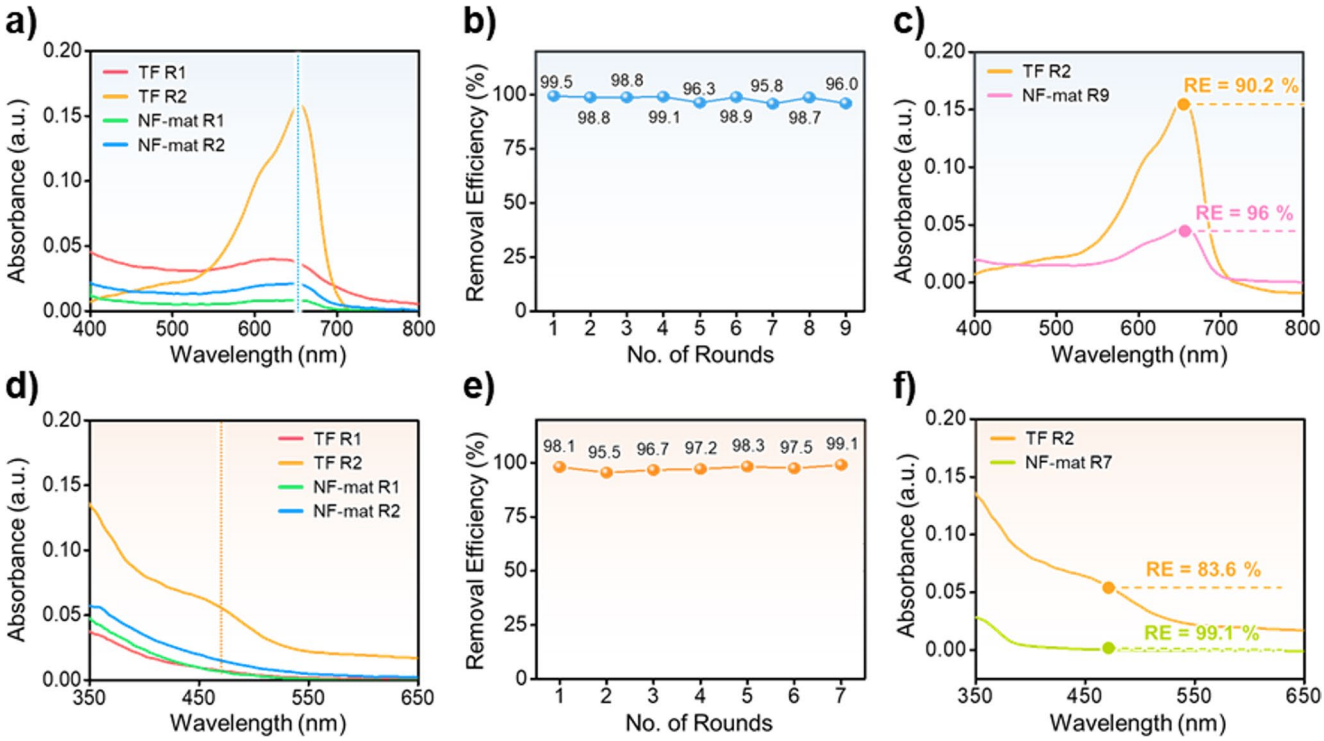

Fig. 7 Recyclability comparison of NF-mat versus TF. **(a)** UV-visible spectra comparison of TF and NF-mat for the first two rounds treated for MB, and **(b)** cyclic stability of NF-mat for MB. **(c)** Direct comparison of the UV-visible spectra of TF for the recycling round-2 with round-9 of NF-mat for MB. **(d)** UV-visible spectra comparison of TF and NF-mat for the first two rounds treated for MO, and **(e)** cyclic stability of NF-mat for MO. **(f)** Direct comparison of the UV-visible spectra of TF for the recycling round-2 with round-7 of NF-mat for MO

further screen for possible release into the treated solutions, the dye solutions are evaporated and the resulting residues are analyzed by SEM/EDS, as shown in Fig. S20. Fluorine and silicon signals are detected in the dried residues for both R1 and the final rounds; however, the measured contents remain at a trace level (<0.1 atomic %) and are comparable to the untreated-solution blank, indicating that these signals likely reflect background/trace contamination as well as the semi-quantitative limitation of EDS either background/trace contamination or the semi quantitative limitation than measurable material release under the present conditions rather than measurable material release under the present conditions. It is emphasized that SEM/EDS of dried residues provides qualitative/semi-quantitative screening and does not quantify dissolved fluoride (F^-) or total silicon in treated water. Accordingly, dedicated quantitative analyses, such as ion chromatography for dissolved fluoride and inductively coupled plasma-mass spectroscopy for total silicon, will be required in future work to rigorously assess environmental risks associated with PVDF and SiO_2 release.

To highlight the cost benefit associated with recyclability, the levelized cost of water (LCOW; cost per unit volume of treated water), is estimated as shown in Supporting Information. The LCOW analysis indicates that NF-mat recycling substantially reduces the treatment cost compared with the single-use scenario for both MB and MO, demonstrating the economic advantage enabled by the reusability of the NF-mat. It should be noted that the absolute LCOW values are sensitive to laboratory-scale batch conditions and are expected to decrease upon scale-up. Accordingly, further work should focus on process optimization and scale-up to reduce LCOW and improve practical viability, which would also lower the associated carbon footprint by reducing electricity and material demand.

4 Conclusion

In this study, we achieved efficient decolorization of representative azo and thiazine dyes by inducing contact-electro-catalytic reaction with a novel electrospun SiO_2–PVDF NF-mat. Under ultrasonication, continuous LS-CE on the NF-mat promoted ROS generation and enabled effective dye decolorization. Using the NF-mat, MB removal reached 99.5% within 4 h, while MO removal reached 98.1% within 8 h, and the NF-mat could be readily recovered and reused over multiple cycles without any measurable loss of performance. Although MB showed a concurrent adsorption contribution, the removal of both dyes was predominantly governed by ROS-mediated CEC. Although this work

demonstrates rapid decolorization, decolorization does not necessarily imply complete mineralization; therefore, future work will evaluate total organic carbon (and related metrics) and transformation products to verify mineralization and overall environmental safety. Nevertheless, considering its high catalytic reaction efficiency with excellent recyclability, the proposed system offers a promising route for dye treatment, and potentially, for broader oxidation-based applications toward sustainable water treatment and green chemical synthesis.

Supplementary Information The online version contains supplementary material available at https://doi.org/10.1007/s42114-026-01820-9.

Acknowledgements This work was supported by the National Research Foundation of Korea (NRF) grant funded by the Korea government (MSIT) (No. RS-2024-00344920). This work was supported by the National Research Foundation of Korea (NRF) grant funded by the Korea government (MSIT) (RS-2025-00521278). This research was also supported by Basic Research Program through the National Research Foundation of Korea (NRF) funded by the Ministry of Education (No. 2018R1A6A1A03025526). This was also supported by the National Research Foundation of Korea (NRF) funded by the Korean government (MSIT) (RS-2025–00556087). The authors thank the Cooperative Equipment Center at KOREATECH for assistance with SEM-EDS analysis.

Author contributions **Muhammad Awais** : Methodology, Formal analysis, Investigation, Writing – Original Draft**Sunmin Jang** : Conceptualization, Formal analysis, Validation, Writing – Review & Editing**Donghan Lee** : Conceptualization**Sumin Cho** : Validation**Sangeun Lee** : Investigation**Soban Ali Shah** : Formal analysis**Muhammad Ramzan Khawar** : Investigation**Kangmin Yun** : Investigation**Dongik Kam** : Investigation**Juyeong Kim** : Validation**Hee Jae Hwang** : Methodology**Sung Jea Park** : Supervision, Writing – Review & Editing**Dongwhi Choi** : Conceptualization, Supervision, Writing – Review & Editing.

Funding This work was supported by the National Research Foundation of Korea (NRF) grant funded by the Korea government (MSIT) (No. RS-2024-00344920). This work was supported by the National Research Foundation of Korea (NRF) grant funded by the Korea government (MSIT) (RS-2025-00521278). This research was supported by Basic Research Program through the National Research Foundation of Korea (NRF) funded by the Ministry of Education (No. 2018R1A6A1A03025526). This was also supported by the National Research Foundation of Korea (NRF) funded by the Korean government (MSIT) (RS-2025–00556087). The authors thank the Cooperative Equipment Center at KOREATECH for assistance with SEM-EDS analysis.

Data availability The datasets used and/or analysed during the current study available from the corresponding author on reasonable request.

Declarations

Competing interests The authors declare no competing interests.

References

1. Jiang B et al (2022) "Contact-piezoelectric bi-catalysis of an electrospun ZnO@PVDF composite membrane for dye decomposition,." Molecules 27(23):8579. https://doi.org/10.3390/MOLECULES27238579
2. Yadav SC (2024) "Water pollution: the problems and solutions,." Sci Insights 44(2):1245–1251. https://doi.org/10.15354/SI.24.RE905
3. Xu Q, Sun D, Qi Y, Duan L (2019) "Efficient removal of anionic organic dyes from aqueous solution with Cu-organic frameworks,." Chem Eng Technol 42(5):1070–1077. https://doi.org/10.1002/CEAT.201800398
4. Chen X et al (2017) "Fluid eddy induced piezo-promoted photodegradation of organic dye pollutants in wastewater on ZnO nanorod arrays/3D Ni foam,." Mater Today 20(9):501–506. https://doi.org/10.1016/J.MATTOD.2017.08.027
5. Kuru M, Pekdemir S (2020) "Polydopamine mediated growth of Ag nanostructures on ZnO thin films for catalytic degradation of organic dyes,." Gazi Univ J Sci 33(4):857–870. https://doi.org/10.35378/GUJS.646532
6. Gomollón-Bel F (2019) "Ten chemical innovations that will change our world: IUPAC identifies emerging technologies in chemistry with potential to make our planet more sustainable,." Chem Int 41(2):12–17. https://doi.org/10.1515/CI-2019-0203
7. Gaur A, Chauhan VS, Vaish R (2023) "Planetary ball milling induced piezocatalysis for dye degradation using $BaTiO_3$ ceramics,." Environ Sci Adv 2(3):462–472. https://doi.org/10.1039/D2VA00210H
8. Chen Z, Lu Y, Liu X, Li J, Liu Q (2023) "Novel magnetic catalysts for organic pollutant degradation via contact electro-catalysis,." Nano Energy 108:108198. https://doi.org/10.1016/J.NANOEN.2023.108198
9. Li H, Berbille A, Zhao X, Wang Z, Tang W, Wang ZL (2023) "A contact-electro-catalytic cathode recycling method for spent lithium-ion batteries,." Nat Energy 8(10):1137–1144. https://doi.org/10.1038/s41560-023-01348-y
10. Wang Z et al (2022) Contact-electro-catalysis for the degradation of organic pollutants using pristine dielectric powders. Nat Commun 13(1):1–9. https://doi.org/10.1038/s41467-021-27789-1
11. Dong X, Wang Z, Berbille A, Zhao X, Tang W, Wang ZL (2022) Investigations on the contact-electro-catalysis under various ultrasonic conditions and using different electrification particles. Nano Energy 99:107346. https://doi.org/10.1016/J.NANOEN.2022.107346
12. Farrokhbin M, Stojimirović B, Galli M, Khajeh Aminian M, Hallez Y, Trefalt G (2019) Surfactant mediated particle aggregation in

nonpolar solvents. Phys Chem Chem Phys 21(35):18866–18876. https://doi.org/10.1039/C9CP01985E
13. Lohmann R et al (2020) Are fluoropolymers really of low concern for human and environmental health and separate from other PFAS? Environ Sci Technol 54(20):12820. https://doi.org/10.1021/ACS.EST.0C03244
14. Cho S et al (2022) Self-powered hybrid triboelectric–piezoelectric electronic skin based on P(VDF-TrFE) electrospun nanofibers for artificial sensory system. Funct Compos Struct 4(4):045005. https://doi.org/10.1088/2631-6331/aca139
15. Kim B et al (2022) High-performance electrospun particulate matter (PM) filters embedded with self-polarizable tetragonal BaTiO3 nanoparticles. Chem Eng J 450(2):138340. https://doi.org/10.1016/j.cej.2022.138340
16. Kumarage S, Munaweera I, Kottegoda N (2022) A comprehensive review on electrospun nanohybrid membranes for wastewater treatment. Beilstein J Nanotechnol 13(1):137–159. https://doi.org/10.3762/BJNANO.13.10
17. Varesano A, Rombaldoni F, Mazzuchetti G, Tonin C, Comotto R (2010) Multi-jet nozzle electrospinning on textile substrates: Observations on process and nanofibre mat deposition. Polym Int 59(12):1606–1615. https://doi.org/10.1002/pi.2893
18. Lee J, Moon S, Lahann J, Lee KJ (2023) Recent progress in preparing nonwoven nanofibers via needleless electrospinning. Macromol Mater Eng 308(9):2300057. https://doi.org/10.1002/mame.202300057
19. Hosseini Ravandi SA, Sadrjahani M, Valipouri A, Dabirian F, Ko FK (2022) "Recently developed electrospinning methods: a review,." Text Res J 92(23–24):5130–5145. https://doi.org/10.1177/00405175211069880
20. Nezarati RM, Eifert MB, Cosgriff-Hernandez E (2013) "Effects of humidity and solution viscosity on electrospun fiber morphology,." Tissue Eng Part C Methods 19(10):810–819. https://doi.org/10.1089/ten.tec.2012.0671
21. Zhang H et al (2025) "High-durability polydimethylsiloxane/quartz@SiO2 superhydrophobic coating with enhanced mechanical robustness and wear resistance,." Polym Test 152(5):108967. https://doi.org/10.1016/j.polymertesting.2025.108967
22. Shenoy SL, Bates WD, Frisch HL, Wnek GE (2005) "Role of chain entanglements on fiber formation during electrospinning of polymer solutions: good solvent, non-specific polymer–polymer interaction limit,." Polymer (Guildf). 46(10):3372–3384. https://doi.org/10.1016/j.polymer.2005.03.011
23. Brettmann BK, Tsang S, Forward KM, Rutledge GC, Myerson AS, Trout BL (2012) "Free surface electrospinning of fibers containing microparticles,." Langmuir 28(25):9714–9721. https://doi.org/10.1021/la301422x
24. Jin Y et al (2024) "How liquids charge the superhydrophobic surfaces,." Nat Commun 15(1):4762-. https://doi.org/10.1038/s41467-024-49088-1
25. Grau-Marin D, Silvestre-Albero J, Jardim EO, Jagiello J, Betz WR, Peña LE (2020) "Evaluation of the textural properties of ultramicroporous carbons using experimental and theoretical methods,." Carbon 157:495–505. https://doi.org/10.1016/J.CARBON.2019.10.035
26. da Silva FE, Rigoti E, de Mello MIS, Pergher SBC (2024) "Tuning textural properties by changing the morphology of SBA-15 mesoporous materials,." Materials 17(12):2827. https://doi.org/10.3390/MA17122827/S1
27. Zhao X, Su Y, Berbille A, Wang ZL, Tang W (2023) "Degradation of methyl orange by dielectric films based on contact-electrocatalysis,." Nanoscale 15(13):6243–6251. https://doi.org/10.1039/D2NR06783H
28. Cui X et al (2022) Greatly enhanced tribocatalytic degradation of organic pollutants by TiO_2 nanoparticles through efficiently harvesting mechanical energy. Sep Purif Technol 289:120814. https://doi.org/10.1016/J.SEPPUR.2022.120814
29. Li P et al (2019) Strong tribocatalytic dye decomposition through utilizing triboelectric energy of barium strontium titanate nanoparticles. Nano Energy 63:103832. https://doi.org/10.1016/J.NANOEN.2019.06.028
30. Wang Z et al (2024) A contact-electro-catalysis process for producing reactive oxygen species by ball milling of triboelectric materials. Nat Commun 15(1):1–10. https://doi.org/10.1038/S41467-024-45041-4
31. do Nascimento Moraes Calazans TR et al (2024) Methylene blue removal using a nanomagnetic support: a response surface approach. Nanoscale Adv 6(15):3887–3894. https://doi.org/10.1039/D4NA00318G
32. O. Ovchinnikov, A. Evtukhova, … T. K.-V., and undefined 2016, Manifestation of intermolecular interactions in FTIR spectra of methylene blue molecules, *Elsevier*, Accessed: Oct. 16, 2025. [Online]. Available: https://www.sciencedirect.com/science/article/pii/S0924203116301230
33. Li Z, Wang CJ, Jiang WT (2010) Intercalation of methylene blue in a high-charge calcium montmorillonite - an indication of surface charge determination. Adsorpt Sci Technol 28(4):297–312. https://doi.org/10.1260/0263-6174.28.4.297
34. Ederer J et al (2022) A study of methylene blue dye interaction and adsorption by monolayer graphene oxide. Adsorpt Sci Technol. https://doi.org/10.1155/2022/7385541
35. K. Imamura, E. Ikeda, T. Nagayasu, … T. S.-J. of colloid and, and undefined 2002,Adsorption behavior of methylene blue and its congeners on a stainless steel surface,*ElsevierK Imamura, E Ikeda, T Nagayasu, T Sakiyama, K NakanishiJournal of colloid and interface science, 2002•Elsevier*, Accessed: Oct. 16, 2025. [Online]. Available: https://www.sciencedirect.com/science/article/pii/S0021979701979676
36. S. de A. Nicolai, … P. R.-J. of, and undefined 2002, Electrochemical and spectroelectrochemical(SERS) studies of the reduction of methylene blue on a silver electrode, *Elsevier*, Accessed: Oct. 16, 2025. [Online]. Available: https://www.sciencedirect.com/science/article/pii/S002207280200832X
37. Ralaiarisoa M et al (2023) In situ investigation of ion exchange membranes reveals that ion transfer in hybrid liquid/gas electrolyzers is mediated by diffusion, not electromigration. J Mater Chem A 11(25):13570–13587. https://doi.org/10.1039/D3TA02050A
38. Wang J, Tan Y, Yang H, Zhan L, Sun G, Luo L (2023) On the adsorption characteristics and mechanism of methylene blue by ball mill modified biochar. Sci Rep 13(1):21174. https://doi.org/10.1038/s41598-023-48373-1
39. Li H, Budarin VL, Clark JH, North M, Wu X (2022) Rapid and efficient adsorption of methylene blue dye from aqueous solution by hierarchically porous, activated starbons®: mechanism and porosity dependence. J Hazard Mater 436:129174. https://doi.org/10.1016/J.JHAZMAT.2022.129174
40. Zhang J, Zhang Y, Lei Y, Pan C (2011) Photocatalytic and degradation mechanisms of anatase TiO2: a HRTEM study. Catal Sci Technol 1(2):273–278. https://doi.org/10.1039/C0CY00051E
41. Alghamdi AA et al (2019) Adsorption of azo dye methyl orange from aqueous solutions using alkali-activated polypyrrole-based graphene oxide. Molecules 24(20):3685. https://doi.org/10.3390/MOLECULES24203685
42. Sun M, Lu Q, Wang ZL, Huang B (2021) Understanding contact electrification at liquid–solid interfaces from surface electronic structure. Nat Commun 12(1):1–11. https://doi.org/10.1038/s41467-021-22005-6
43. Lin S, Xu L, Wang AC, Wang ZL (2020) Quantifying electron-transfer in liquid-solid contact electrification and the formation of

electric double-layer. Nat Commun 11(1):1–8. https://doi.org/10.1038/s41467-019-14278-9
44. Encyclopedia of Physical Science and Technology | ScienceDirect Accessed: Mar. 04, 2026. [Online]. Available: https://www.sciencedirect.com/referencework/9780122274107/encyclopedia-of-physical-science-and-technology
45. Lim KH, Sun Y, Lim WC, Soh S (2020) Charging organic liquids by static charge. J Am Chem Soc 142(50):21004–21016. https://doi.org/10.1021/jacs.0c06000
46. Choi D et al (2013) Spontaneous electrical charging of droplets by conventional pipetting. Scientific Reports 3(1):2037. https://doi.org/10.1038/srep02037
47. Xu P, Wang H, Tong R, Du Q, Zhong W (2006) Preparation and morphology of SiO2/PMMA nanohybrids by microemulsion polymerization. Colloid and Polymer Science 284(7):755–762. https://doi.org/10.1007/s00396-005-1428-9
48. Study on the structural design and performance of novel braid-reinforced and thermostable poly(m -phenylene isophthalamide) hollow fiber membranes - RSC Advances (RSC Publishing) DOI:10.1039/C7RA01171G. Accessed: Mar. 04, 2026. [Online]. Available: https://pubs.rsc.org/en/content/articlehtml/2017/ra/c7ra01171g
49. Wang Y et al (2021) Ultrasonic activation of inert poly(tetrafluoroethylene) enables piezocatalytic generation of reactive oxygen species. Nature Communications 12(1):3508. https://doi.org/10.1038/s41467-021-23921-3
50. Yoo D, Jang S, Cho S, Choi D, Kim DS (2023) A liquid triboelectric series. Advanced Materials 35(26):2300699. https://doi.org/10.1002/adma.202300699
51. Sosa MD, D'Accorso NB, Martínez Ricci ML, Negri RM (2022) Liquid–polymer contact electrification: modeling the dependence of surface charges and ξ-potential on pH and added-salt concentration. Langmuir 38(29):8817–8828. https://doi.org/10.1021/acs.langmuir.2c00813
52. Hayyan M, Hashim MA, Alnashef IM (2016) Superoxide ion: generation and chemical implications. Chem. Rev. 116(5):3029–3085. https://doi.org/10.1021/ACS.CHEMREV.5B00407/ASSET/IMAGES/MEDIUM/CR-2015-004079_0040.GIF
53. Liang P, Yang W, Peng H, Zhao S (2024) Efficient degradation of methylene blue in industrial wastewater and high cycling stability of nano ZnO. Molecules 29(23):5584. https://doi.org/10.3390/MOLECULES29235584
54. Manori S et al (Jan. 2025) Radical-mediated photocatalytic dye degradation and antimicrobial properties of La2NiMnO6 nanoparticles. New J Chem 49(3):807–824. https://doi.org/10.1039/D4NJ04437A
55. Jinga LI (2021) Chemical degradation of Methylene Blue dye using TiO2/Au nanoparticles. Nanomaterials Basel 11(6):1605. https://doi.org/10.3390/NANO11061605
56. Neli Ö (2026) Enhancing Methyl Orange dye degradation via photoelectrocatalytic and electrocatalytic methods: a novel composite electrode approach utilizing Pt-loaded hybrid metal oxides. Mater Chem Phys 350:131940. https://doi.org/10.1016/J.MATCHEMPHYS.2025.131940
57. Liyanaarachchi H, Thambiliyagodage C, Lokuge H, Vigneswaran S (2023) Kinetics and thermodynamics study of Methylene Blue adsorption to Sucrose- and Urea-derived nitrogen-enriched, hierarchically porous carbon activated by KOH and H3PO4. ACS Omega 8(18):16158–16173. https://doi.org/10.1021/ACSOMEGA.3C00339
58. Sahu S (2020) Adsorption of Methylene Blue on chemically modified lychee seed biochar: dynamic, equilibrium, and thermodynamic study. J Mol Liq 315:113743. https://doi.org/10.1016/J.MOLLIQ.2020.113743
59. Kgatle M, Sikhwivhilu K, Ndlovu G, Moloto N (2021) Degradation kinetics of Methyl Orange dye in water using trimetallic Fe/Cu/Ag nanoparticles. Catalysts Basel 11(4):428. https://doi.org/10.3390/CATAL11040428
60. Keen O, Bolton J, Litter M, Bircher K, Oppenländer T (2018) Standard reporting of electrical energy per order (EEO) for UV/H2O2 reactors (IUPAC technical report). Pure Appl Chem 90(9):1487–1499. https://doi.org/10.1515/pac-2017-0603
61. Ahn Y, Lee D, Kwon M, hwan Choi I, Nam SN, Kang JW (Aug. 2018) Evaluation of advanced oxidation processes for water and wastewater treatment – A critical review. Water Res 139:118–131. https://doi.org/10.1016/j.chemosphere.2017.06.079
62. Degradation of methyl orange by dielectric films based on contact-electro-catalysis - Nanoscale (RSC Publishing) DOI:10.1039/D2NR06783H. Accessed: Mar. 05, 2026. [Online]. Available: https://pubs.rsc.org/en/content/articlehtml/2023/nr/d2nr06783h
63. Wei P et al (2024) Low-frequency ultrasound assisted contact-electro-catalysis for efficient inactivation of *Microcystis aeruginosa*,. J Hazard Mater 478:135537. https://doi.org/10.1016/j.jhazmat.2024.135537
64. Cao DQ et al (2024) Contact-electro-catalysis for degradation of trace antibiotics in wastewater,. Chem Eng J 487(16):150531. https://doi.org/10.1016/j.cej.2024.150531
65. Duan Y, Yu J (2024) Improving reactive oxygen species generated from micro-nano bubbles by hydrophobic catalytic ceramic membrane for wastewater treatment,. Chem Eng J 500:157206. https://doi.org/10.1016/J.CEJ.2024.157206